Published in final edited form as:
Acta Biomater. 2022 January 15; 138: 313–326. doi:10.1016/j.actbio.2021.11.005.

Tungsten disulfide nanotubes enhance flow-induced crystallization and radio-opacity of polylactide without adversely affecting in vitro toxicity

Karthik Ramachandran[a,§,†], **Zixuan Shao**[a,§,‡], **Tiziana Di Luccio**[a,b,§], **Bo Shen**[a], **Edgar E. Ruiz Bello**[a,c], **Loredana Tammaro**[b], **Fulvia Villani**[b], **Fausta Loffredo**[b], **Carmela Borriello**[b], **Francesca Di Benedetto**[d], **Eimear Magee**[e], **Tony McNally**[e], **Julia A. Kornfield**[a,*]

[a]Division of Chemistry and Chemical Engineering, California Institute of Technology, 1200 E California Blvd, Pasadena CA, 91125, USA

[b]Division of Sustainable Materials, ENEA Centro Ricerche Portici, Piazzale E. Fermi 1, Portici, 80055, Italy

[c]Department of Chemical Engineering, University of Guanajuato, Lomas del Bosque103, Lomas del Campestre, 37150 León, Gto, Mexico

---

[*] corresponding author: kornfield@cheme.caltech.edu.

[§] contributed equally

[†] Present address: Moderna, Cambridge, MA - 02062

[‡] Present address: Allegro Ophthalmics, LLC, San Juan Capistrano, CA - 92675

Declaration of Competing Interests
There are no conflicts of interests to declare.

Supplementary Material
Scanning electron microscopy (Fig. S1) elucidates the aspect ratio of WS_2 nanotubes and ZnO nanoparticles. Gel permeation chromatography quantifies changes in molecular weight (M_w) of compression molded PLA, PLA-WS_2 (0.05%) and PLA-WS_2 (0.1%) ingots and sheared samples relative to the as-received PLA resin (Figs. S2–S3). PLA and PLA nanocomposite (WSNT and ZnO) disks were prepared from solvent-cast and successively hot pressed films (Fig. S4) for biocompatibility assays. Phase contrast micrographs of HUVECs and HASMCs exposed to WSNT at 5.9 μg/cm^2 for 24hrs show endocytosed WSNT with similar morphology before and after washing (Fig. S7). Phase contrast micrographs of HASMCs and HUVECs (Fig. S9, S10) exposed to a 1.5–29.2 μg/cm^2 concentration series of bare WSNT and ZnO nanoparticles illustrate the toxicity of ZnO relative to WSNT. Live/Dead staining images of HUVECs and HASMCs after 24 hrs of treatment with bare nanoparticles (Fig. S8, S11) are consistent with phase contrast microscopy. A time course cell viability assay for HUVECs and HASMCs tracks the metabolic activity of these cells exposed to bare nanoparticles and nanocomposite disk-treated media after 24 hrs (Fig. S12) and up to 72 hrs treatment (Fig. S13). Phase Contrast micrographs of HUVECs and HASMCs at the nanocomposite disk edge show consistent cell density at the film interface after 24 hours of exposure (Fig. S14). TEM images of HASMCs and HUVECs exposed to 5.9 μg/cm^2 WSNT for 24 hrs are shown in Fig. S15A and S15B, respectively.
The in situ retardance profiles during and after cessation of flow for PLA and PLA-WSNT subjected to varying shear temperature are reported in Fig. S16. The temperature and pressure traces corresponding to the *in situ* retardance data in Fig. 4 and Fig. S16 are reported in Fig. S17. The material extruded from each shear experiment (Fig. S18A) enables calculation of the wall shear rate (Fig. S18B). The *in situ* retardance data presented in Fig. 4 and Fig. S16 are extracted from normalized intensity profiles (Fig. S19–S21). To complement Fig. 5, Fig. S24 and S25 present polarized light micrographs of PLA/PLA-WSNT sections at different angles relative to the polarizer and analyzer of the microscope. Wide angle X-ray scattering data for PLA (Fig. S26), PLA-WSNT 0.05 wt% (Fig. S27) and PLA-WSNT 0.1 wt% (Fig. S28) provide more insight on the unusual morphology observed in the polarized light micrographs of the PLA/PLA-WSNT sections. The SM also describes the calculation of the wall shear rate, average spacing between WSNT in PLA, birefringence from WSNT and the quantification of the upturn and residual retardance (Fig. S22, S23).

Declaration of interests
The authors declare that they have no known competing financial interests or personal relationships that could have appeared to influence the work reported in this paper.

[d]Division of Sustainable Materials, ENEA Centro Ricerche Brindisi, SS7 Appia Km 706, Brindisi, 72100, Italy

[e]International Institute for Nanocomposites Manufacturing (IINM), WMG, University of Warwick, CV4 7AL, UK

Abstract

Treatment of vascular disease, from peripheral ischemia to coronary heart disease (CHD), is poised for transformation with the introduction of transient implants designed to “scaffold” regeneration of blood vessels and ultimately leave nothing behind. Improved materials could expand the use of these devices. Here, we examine one of the leading polymers for bioresorbable scaffolds (BRS), polylactide (PLA), as the matrix of nanocomposites with tungsten disulfide (WS_2) nanotubes (WSNT), which may provide mechanical reinforcement and enhance radio-opacity. We evaluate *in vitro* cytotoxicity using vascular cells, flow-induced crystallization and radio-opacity of PLA-WSNT nanocomposites at low WSNT concentration. A small amount of WSNT (0.1 wt%) can effectively promote oriented crystallization of PLA without compromising molecular weight. And radio-opacity improves significantly: as little as 0.5 to 1 wt% WSNT doubles the radio-opacity of PLA-WSNT relative to PLA at 17 keV. The results suggest that a single component, WSNT, has the potential to increase the strength of BRS to enable thinner devices and increase radio-opacity to improve intraoperative visualization. The *in vitro* toxicity results indicate that PLA-WSNT nanocomposites are worthy of investigation *in vivo*. Although substantial further preclinical studies are needed, PLA-WSNT nanocomposites may provide a complement of material properties that may improve BVS and expand the range of lesions that can be treated using transient implants.

Graphical abstract

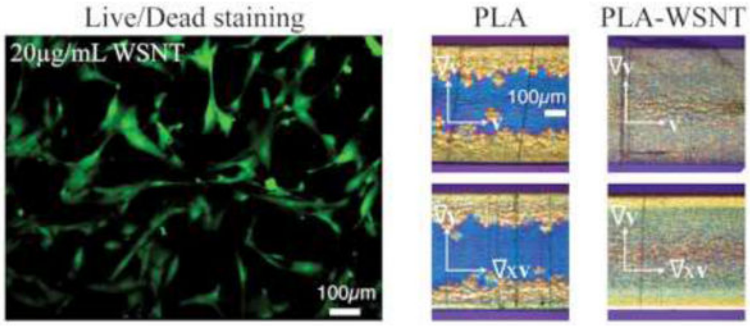

Keywords

Polylactide (PLA); tungsten disulfide (WS_2) nanotubes; flow-induced crystallization; biocompatible nanocomposites; Coronary Heart Disease; Bioresorbable Vascular Scaffolds (BVS)

---

1. Introduction

Vascular disease has significant impact on life expectancy and quality of life. Coronary heart disease (CHD) is one of the leading causes of death in the world [1,2]. Peripheral ischemia, particularly in the legs, impairs mobility and can lead to amputation as disease progresses [3,4]. In view of the broad range in blockage types and vessel sizes [5], we are motivated to expand the range of materials available for bioresorbable scaffolds (BRS). Devices that restore blood flow through an occluded coronary artery are the subject of intense research to reduce complications, both for drug-eluting metal stents (DES) [5], bioresorbable metal stents [6,7] and bioresorbable scaffolds (BRS) [8,9]. Improvements in DES are reducing the incidence of late stent thrombosis [5]. At the same time, Bioresorbable Vascular Scaffolds (BVS), made entirely out of a biodegradable polymer such as polylactide (PLA)[§] [10–12] have been developed to restore arterial vasomotion and eliminate the risk of Late Stent Thrombosis (LST) [13–16]. However, a variety of adverse effects have been observed [17–20] leading to an FDA warning about an increased rate of major cardiac events [21] followed by the withdrawal of the ABSORB BVS from the market (Sept. 2017). Clinicians speculate that the greater thickness of BVSs (~150 μm) relative to metal stents (~80 μm) needed to achieve comparable mechanical properties [22] perturbs the flow of blood, possibly contributing to increased risk of thrombosis [14]. Surgeons also find it challenging to implant a BVS under X-ray guidance as PLA lacks X-ray contrast relative to blood and vascular tissue. The difficulty “seeing” the BVS during implantation may result in incomplete scaffold apposition [23], which could contribute to increased thrombosis risk. A stronger material with greater X-ray contrast might improve BVS safety and expand the range of lesions that they can address: (1) reducing the thickness of BVS might mitigate thrombosis related to irregular blood flow and enable treatment of smaller or more tortuous vessels; and (2) increasing the radio-opacity of BVS to improve visualization with X-rays might mitigate thrombosis resulting from malapposition.

The key to a thinner BVS is a stronger, less brittle material: it must achieve radial strength comparable to the clinically-approved 150 μm BVS in a thinner profile. PLA can be made tougher via blending with other polymers [24–26] or copolymerization [27–29] but these methods can lead to premature loss of radial strength due to accelerated degradation in the body [30,31]. As an alternative, we consider nanotubes as reinforcing agents. We sought nanotubes that might ultimately be tolerated in the body and provide strong X-ray absorption to address the dual challenge of a thinner, radio-opaque vascular scaffold [32]. While Period 3 metals (Mg, Al) and Period 4 metals (e.g., Ti, Cr, Mn, Fe, Co, Ni and Zn) lack of sufficient radio-opacity, Period 6 elements (W, Au and Pt) are promising [33]. Despite the fact that medical implants made of pure tungsten release tungsten into the blood stream as they corrode [34,35], studies on patients who received implanted tungsten embolization coils have revealed no toxicity in adult and pediatric patients [34,36–39]. The literature lead us to the mineral tungstenite (tungsten disulfide, WS_2) for four reasons: methods to create high aspect ratio particles are well established (WS_2 nanotubes, WSNT) [40,41], WSNT disperse readily in PLA (among other polymers) without any surface modification [42,43], 0.5 wt% of WSNT increases the elastic modulus, yield strength and strain at failure of extruded PLA by 20%, 23% and 35%, respectively [44] and WS_2 nanoparticles show promising biocompatibility *in vitro* [45–47]. The high-aspect ratio (30–150 nm diameter, 1–20 μm

---

[§] Poly L-lactide (PLLA) is the medical grade of PLA employed in the manufacturing of BRS, while PLA (with a 2% of D-lactide) has been used in this work. For sake of simplicity, we use the acronym PLA everywhere in the text.

length, [44]) of WSNT is expected to favor preferential orientation along the hoop-direction of the BVS during tube expansion, the first step of BVS processing where a nearly radial deformation is applied to an extruded PLA tube. Surprisingly, we found that the WSNT remain mainly oriented along the axial direction of the initial extruded tube while PLA crystals orient along the hoop direction (as neat PLA) [48]. Although favoring nucleation of PLA crystals, the nanotubes do not perturb their orientation.

Kinetically-controlled morphology and specialized processing methods for BVS give PLA unusual ductility, strength and toughness that lead to the first clinically-approved BVS [49,50]. Moreover, nanoparticles are known to alter the kinetics and morphology development during processing, particularly in semicrystalline polymers [51,52] motivating the present study of the effects of WSNT on the flow-induced crystallization of polylactide (PLA, <2% D-content). We study the development of PLA structure in real time under shear flow by capturing the inception of thread-like precursors that ultimately dictates the oriented PLA morphology (shish-kebabs). *In situ* rheo-optical measurements fill a gap in knowledge: the scant literature on injection-molded PLA only reports the final state of the material. We complement the *in situ* optical measurements with *ex situ* microscopy and X-ray scattering to provide deeper insight on the impact of WSNT on the PLA morphology both during and post flow. Guided by prior literature showing that 0.1 wt% of WSNT boost the compressive strength of poly(propylene fumarate) (PPF) by over 50% [53], we examine two concentrations (0.05 and 0.1 wt%) of WSNT in PLA. These low concentrations of WSNT permit real time optical measurements during and after flow, and *ex situ* optical microscopy.

We assess biocompatibility over the range from 100% WSNT (cells in direct contact with bare nanotubes) to the low concentration used for investigating process-induced morphology (cells in direct contact with PLA-WSNT 0.1 wt% nanocomposite). Clinically, blood has limited contact with the BVS (particularly the structural core as opposed to the drug-eluting layer). The device becomes enveloped in endothelial and smooth muscle cells [54] within the first few months (little degradation of the clinically-approved scaffold is observed even at 6 months, i.e. <5% loss of its initial mass [55]). Therefore, we performed initial *in vitro* cytotoxicity assays of PLA-WSNT nanocomposite and WSNT nanotubes using human endothelial cells from the human smooth muscle cells from the aorta (HASMC) and umbilical vein (HUVEC).

2. Materials and Methods

2.1 Preparation of nanoparticles

Tungsten disulfide (WS_2) nanotubes (WSNT) were purchased from NanoMaterials, Israel. Before use, the WSNT were sonicated and centrifuged to eliminate agglomerates and small impurities (e.g. broken nanotubes) using the following procedure. First, 200 mg of WSNT were dispersed in 200 mL of isopropyl alcohol; the resulting solution was then sonicated at 40 KHz frequency in a flask for 2 hours. Second, the sonicated solution was decanted into falcon tubes (leaving behind the sediment in the flask) and centrifuged at 1500 rpm for 15 minutes. Third, the supernatant was discarded and the pellet of WSNT was dried in the falcon tubes by placing them in a water bath at 50–60 °C for a few days until the WSNT were completely dry and ready to use. The dimensions of the nanotubes after the sonication and centrifuge procedure were ~ 70–200 nm in diameter and 2–3 μm in length (Fig. S1A). Zinc Oxide (ZnO) nanoparticles (catalogue #: 544906, Sigma-Aldrich) (Fig. S1B) were used as a negative control in cytotoxicity experiments. For cell culture, the nanoparticles (WSNT and ZnO) were sterilized by UV light overnight before they were suspended in media using a combination of sonication and vortexing. Residual aggregates were filtered out using a cell strainer with a 40 μm pore size. The nanoparticle-media mixture was then aliquoted to cell culture wells to reach the desired final treatment dose.

2.2 Preparation of nanocomposite films

This study uses polylactide (PLA) with ~ 2% D-content [56,57] and M_w ~ 125 kg/mol (values in Fig. S2; gel-permeation chromatograms in Fig. S3) purchased from NatureWorks, USA (Grade 4032D). The PLA pellets were first dried under vacuum at 80 °C for 1 day and subsequently at 40 °C for an additional 4 days. The vacuum-dried polymer was then dissolved in chloroform at 60 °C for 2 hours. Separately, a suspension of WSNT (0.05 or 0.1 wt%) in chloroform was sonicated for ~ 30 mins to break up nanotube agglomerates preserving the size of the nanotubes post-sonication and centrifuge. The suspension of WSNT was then added to the polymer solution and stirred for an additional 1 hour; the resulting solution was cast into glass petri dishes, covered and allowed to dry inside a fume-hood for ~ 2 days; the as-cast films were placed in a vacuum oven and dried for ~ 4 days at 80 °C to remove residual solvent. The crystalline, as-cast films were thereafter hot-pressed by a Carver hot-press at 180 °C for 10 min to obtain ~100 μm thick, amorphous films that were maintained at 40 °C under vacuum until further use.

2.3 SEM of nanoparticles

Scanning electron micrographs of WSNT and ZnO nanoparticles (Fig. S1) were acquired on a ZEISS 1550VP Field Emission SEM with an electron accelerating voltage of 10 kV. The SEM samples were prepared using the following protocol: (1) disperse 7.2 mg of WSNT (previously sonicated and centrifuged according to the above procedure) or as-received ZnO in 12 mL of chloroform, (2) sonicate the dispersion for 20 minutes to break-up agglomerates and (3) drop-cast the sonicated solution (~0.5 mL) on a silicon wafer for imaging.

2.4 Cell culture

Pooled, Normal, Primary Umbilical Vein Endothelial Cells (HUVECs, ATCC PCS-100–013) and Normal Human Primary Aortic Smooth Muscle Cells (HASMCs, ATCC PCS-100–012) were obtained from the American Type Culture Collection (ATCC). HUVECs were grown in Vascular Cell Basal Medium with Endothelial Cell Growth Kit-BBE additive (ATCC). HASMCs were grown in Vascular Cell Basal Medium with Vascular Smooth Muscle Cell Growth Kit additive (ATCC). P5 to P7 HUVECs and P4 to P6 HASMCs were used in all cell culture experiments. All cell cultures were grown in a humidified incubator at 37 °C with 5% carbon dioxide to control media pH.

2.5 Preparation of PLA, PLA-WSNT and PLA-ZnO disks and treatment of cell culture

Disks (diameter: 22 mm) were cut from hot-pressed PLA, PLA-WSNT (0.1 wt%) and PLA-ZnO (0.1 wt%) films and the central portion (inner diameter: 6 mm) was cut out to facilitate exchange of oxygen and nutrients within the well (Fig. S4A–B). The disks were then sterilized through stringent washes in a 70% Ethanol, 30% water solution followed by drying in a stream of sterile air. The dried disks were then inserted into 12-well cell culture plates containing seeded cells to start the treatment (Fig. S4C). At end of the treatment, the disks were carefully removed to facilitate assay reagent diffusion during WST-1 assay and Live/Dead staining.

2.6 Nanoparticle treatment of cell culture

Nanoparticles (either WSNT or ZnO) were dispersed in media (either HUVEC or HASMC): 1 mg of dry nanoparticles was weighed into a vial and sterilized under UV light overnight prior to addition of 1 mL of media, then a combination of sonication and vortexing was used to disperse the nanoparticles. Cell cultures (described above) in 12-well cell culture plates (22 mm dia.) containing 1 mL of media were given 110 μL combined volume of media and media containing dispersed nanoparticles to final well nanoparticle concentrations of 0, 5, 10, 20, 50, 100 μg/mL to start the treatment. The dose is labeled according to the mass of nanoparticles per mL of media in the well; however, the nanoparticles settle to the bottom and are in *direct contact* with the cells during most of the treatment time (equivalent to 0, 1.5, 2.9, 5.9, 14.6, 29.2 μg/cm^2, respectively). In the time course cell viability assay (Fig. S13), 96-well plates were used instead, with 100 μL of media per well and 11 μL of media containing nanoparticle added.

2.7 WST-1 assay

At the end of a specified treatment time (24, 48 or 72 hours), the WST-1 (water soluble tetrazolium with iodo, nitro and disulfo functional groups) cell proliferation reagent (Roche) was added to the cell culture media at the recommended working concentration and subsequently incubated for four hours at 37 °C. After incubation, 100 μL of the solution was transferred to each well of the 96-well plate for plate-reading using a Flexstation 3 microplate reader (440 nm and 690 nm). The baseline absorption from the background and media was subtracted to isolate the contribution due to the WST-1 assay. All test wells were then normalized by the mean control well value (controls are untreated cells in the case of nanoparticles, and wells that received PLA disks free of nanoparticles in the case of disk overlay). In the bare nanoparticle concentration and time series experiments, statistical tests were performed between the control and treated cells. In the disk overlay experiment, statistical tests were performed between cells exposed to PLA films and other conditions. A 10x Lysis Buffer (Thermo Scientific Pierce) was used as a lethal control (cells were treated for 15 mins prior to the WST-1 assay). For the time series experiments, each disk was incubated with 1 mL of the appropriate growth media for 24 hours in a humidified incubator maintained at 37 °C. Cells were then exposed to this pre-conditioned media (growth media that was in contact with the disks) and their viability was assessed via WST-1 at three different time points (24, 48 and 72 hours).

2.8 Live/Dead staining and phase-contrast microscopy

The LIVE/DEAD Viability/Cytotoxicity Kit (Invitrogen) was used to simultaneously capture the status of both dead and live cells. At start of the assay, cells were washed once with Dulbecco’s Phosphate-Buffered Saline (DPBS) before incubation for 30 minutes at 37 °C in the media-dye mixture. At end of incubation, cells were washed with DPBS and imaged on a Zeiss Axiovert 25CFL microscope. The FIJI software package was used to merge fluorescent signals into one image with red indicating dead cells and green indicating live cells. Phase contrast images were captured on the same microscopy system with bright-field illumination (see Fig. S7 for phase contrast micrographs of the cells before and after the wash). A 10x Lysis Buffer (Thermo Scientific Pierce) was used as the lethal control and was added to wells for 15 minutes before Live/Dead staining.

2.9 TEM of cells cultured with WSNT

Cells were grown in 100 mm cell culture plates to near 50% confluency before treatment with 5.9 $\mu g/cm^2$ of WSNT. After 24 hours of treatment, the cells were washed with Cacodylate buffer and fixed with a 3% glutaraldehyde and 1% paraformaldehyde fixative solution. The cells were then gently scraped off and post-fixed with 2% Osmium Tetroxide, 0.7% Potassium ferrocyanide in Cacodylate buffer. After post-fix, the cells were washed with additional Cacodylate buffer and distilled water before en bloc staining with 1% aqueous uranyl acetate. Finally, the cells were dehydrated with an acetone gradient series, infiltrated into an Epon-Araldite resin and transferred to embedding molds for polymerization. Semi-thick 400 nm sections of the samples were cut with a UC6 Ultramicrotome (Leica Microsystems) using a diamond knife (Diatome, Ltd.). The sections were placed on formvar-coated, copper-rhodium 2 mm slot grids and stained with 3% uranyl acetate and lead citrate. The grids were placed in a dual-axis tomography holder (Model 2040, EA Fischione Inc.) and imaged with a Tecnai TF30ST transmission electron microscope (ThermoFisher Scientific) at 300 keV. Images were recorded digitally with a US1000 CCD camera (Gatan, Inc.). Tomographic tilt-series data were acquired as described in the literature [58]. Briefly, the grids were tilted ±64° and images were acquired in 1° increments. The grid was then rotated 90° and a similar series was taken about the orthogonal axis. Tomographic data and projection images were processed and analyzed using the IMOD software [59,60] package on a MacPro Computer (Apple, Inc).

2.10 Statistical analysis

All biocompatibility statistical tests were performed in GraphPad Prism 7.00. The variation in cellular viability between different conditions was tested using two-way ANOVA for WST-1 assays (statistical significance threshold set at $p\text{-value} < 0.05$). In the nanoparticle concentration and time series studies, statistical tests were performed against untreated cells. In the disk overlay study, statistical tests were performed against cells exposed to PLA.

2.11 Preparation of PLA and PLA-WSNT ingots

Vacuum dried PLA pellets and PLA-WSNT films were compression-molded into an ~8 g cylindrical “ingot”, which is the starting material for the flow-induced crystallization experiments described below. Heat and pressure were applied to the mold using a Carver hot-press. The two platens of the hot-press were maintained at 200 °C and the temperature of the mold was continuously recorded using a thermocouple in contact with its inner wall. The mold was also connected to a vacuum line (< 300 mTorr) to remove any moisture that can induce degradation of PLA near the melt. The mold was heated to 180 °C and held at that temperature for 10 mins under a pressure of ~2 tonnes. The mold was then removed from the hot-press and rapidly quenched to ~60 °C in dry ice. The ingot was subsequently extracted from the mold and stored under vacuum at 40 °C.

2.12 In situ flow induced crystallization (FIC)

A custom-built apparatus (see schematics in Fig. S5) [61] was used to probe the impact of WSNT on the microstructure of PLA during flow. PLA and PLA-WSNT ingots were first placed in the instrument's reservoir, which was maintained at 200 °C, above the melting temperature of PLA (T_m ~ 170 °C, differential scanning calorimetry analyses reported in Fig. S6). A pressure-driven piston was used to transfer PLA from the reservoir into a narrow rectangular capillary (6.35 cm x 6.35 mm x 500 μm) termed the "shear cell". The lowest possible pressures were used during filling to avoid pre-orientation of PLA. The shear cell was then maintained at 200 °C for an additional 5 minutes to erase thermal history. Using a recirculating oil bath, the shear cell was cooled to the prescribed shear temperature (T_s: 125 – 140 °C) at ~8.5 °C/min and a shear pulse (shear time t_s: 10–40 s; wall shear stress σ_w: 0.11–0.23 MPa) was applied using the aforementioned pneumatic piston. A pressure transducer located near the inlet of the shear cell enabled calculation of the wall shear stress (σ_w; see equation S1) for each experiment. At the outlet of the shear cell, a pair of quartz windows permitted a beam of plane-polarized light (632.8 nm He-Ne laser) to interact with the flowing polymer. The transmitted light comes into contact with a polarizing beam splitter and two detectors that provide real-time measurement (millisecond resolution) of the "retardance", an optical property analogous to birefringence that is sensitive to oriented crystallization.

2.13 Gel permeation chromatography (GPC)

The molecular weight (M_w) of PLA and PLA-WSNT after shearing with the FIC apparatus was measured using a Wyatt DAWN EOS Multi-Angle Light Scattering System (MALLS, λ = 690 nm) in conjunction with a Waters 410 differential refractometer (λ = 930 nm). The system uses degassed tetrahydrofuran (THF) as the mobile phase at a temperature and flow rate of 35 °C and 0.9 mL/min respectively. The samples were first dissolved in THF at a concentration of 5 mg/mL and the resulting solution was filtered through a 0.45 μm pore poly(tetrafluoroethylene) (PTFE) membrane. The filtered solution was injected into the system and separation was achieved (longest molecules elute first) using four Agilent PLgel columns (pore sizes: 10^3, 10^4, 10^5 and 10^6 Å) connected in series. Elution was complete in 50 minutes and data (light scattering and refractive index) were acquired at a resolution of 5 Hz. Data analysis was performed in the Wyatt Astra software (version 5.3.4) using the Zimm fitting formula with dn/dc = 0.042 mL/g for poly L-lactide.

2.14 Sectioning and Microscopy

Sheared PLA and PLA-WSNT samples were first embedded in OCT (optimal cutting temperature) media to facilitate sectioning. The embedded samples were microtomed using

Sakura Finentek's Tissue Tek-Cryo$_3$ into ~ 50 μm thick sections both normal to the flow-direction (∇x**v**–∇**v)** and the vorticity-direction (**v**–∇**v)**. The samples were sectioned at −35 °C to minimize the impact of the stainless-steel knife (Sakura Accu-Edge 4685 blades) on the morphology of the samples. The microtomed sections were subsequently imaged through crossed-linear polarizers in a Zeiss Universal Microscope equipped with a Canon EOS DS30 camera.

2.15 X-ray scattering

The morphology of PLA and PLA-WSNT samples subjected to shear flow was probed using X-rays at beamline 5-ID-D of the Advanced Photon Source (APS), Argonne National Labs. The incident X-ray beam with spot-size 250 μm x 250 μm was aligned parallel to the gradient (∇ **v)**, flow (**v)** and vorticity-direction (∇ x**v)** to obtain a 3D-view of the morphology in each sample. Wide Angle X-ray Scattering (WAXS) patterns were acquired on a Rayonix CCD detector that was located 200.83 mm from the sample. Diffraction patterns were acquired with an exposure time of 0.5 s using X-rays of wavelength 0.7293 Å. Drift in the background scatter was monitored by periodically acquiring "air" scattering patterns (no sample in the path of the beam) at 0.5 s of exposure as well. The air frames were averaged to obtain a single background image that was subtracted from the sample images to isolate the scattering from PLA/PLA-WSNT alone. The subtracted patterns were then normalized by the total number of counts to account for variations in thickness.

2.16 X-ray radio-opacity

The X-ray radio-opacity was evaluated by measuring the X-ray beam transmitted intensity during small angle X-ray scattering experiments at the beamline 5-ID-D at the Advanced Photon Source of the Argonne National Laboratories. The samples under analysis were extruded using a Prism Eurolab 16 mm twin screw extruder (ThermoFisher Scientific, USA) with 10 heating zones set from 140 °C at the feed end to 200 °C at the die and a screw speed of 70 rpm to produce cylindrical pellets (~1.5 mm diameter and 3–4 mm axial length) of neat PLA and PLA-WS$_2$ with nominal concentration of WS$_2$ equal to 0.1, 0.3, 0.5, 1.0 and 3.0 wt%. The pellets were mounted on a cardboard holder and fixed with double side tape at the extremities of ~ 3 mm diameter holes drilled in the cardboard thus allowing the X-ray beam to pass through each sample (Fig. 7A). The beam was aligned perpendicular to the pellet axis; three acquisitions at different axial positions on each sample were recorded every 0.1 s at an exposure time of 0.1 s and then averaged using a beam of energy = 17 KeV (wavelength = 0.7293 Å) with spot size on the sample equal to 250 μm x 250 μm. A photodiode positioned on the beamstop at a distance of 8503 mm from the sample provided the photon counts transmitted by the sample while an ionization chamber positioned before the sample and nearby the incident beam path recorded time-dependent fluctuations of the incident beam. The final transmitted intensity was calculated as the ratio between the transmitted counts and the incident counts, each one diminished by the dark current of the respective detectors, relatively to the incident beam (signals recorded without any sample in the beam).

3. Results

3.1 In vitro biocompatibility assays

In vitro biocompatibility assays were performed for both bare WSNT and PLA-WSNT nanocomposites, with corresponding controls in two cell lines – Human Umbilical Vein Endothelial Cells (HUVECs) and Human Aortic Smooth Muscle Cells (HASMCs), which represent the major cell types that are likely to contact the deployed scaffold in the artery [62]. *In vivo* observations show the device becomes enveloped in endothelial and smooth muscle cells [54] within the first few months, before significant degradation occurs (the clinically-approved scaffold loses <5% of its initial mass in 6 months [55]). We performed a series of cell culture experiments to assess the toxicity of WSNT and the PLA-WSNT nanocomposites. To evaluate toxicity of bare WSNT, we used four methods: phase contrast microscopy [63], Live/Dead staining [64], WST-1 assay [47] and transmission electron microscopy (TEM) [46]. The cytotoxicity of PLA-WSNT nanocomposite films in direct contact with HUVECs and HASMCs for 24 hours was assessed using phase contrast microscopy, Live/Dead staining and WST-1 assays. As an additional test, media that had been incubated with PLA-WSNT nanocomposites for 24 hrs was applied to cells and their metabolic activity was monitored at 24, 48 and 72 hrs.

Consistent with the prior literature on cytotoxicity of WSNT with rat salivary cells [46], human bronchial epithelial cells [47], human hepatocytes [47], and mouse macrophages [47], phase contrast microscopy of HASMCs and HUVECs indicates that both cell lines retain their morphology when exposed to direct contact with WSNT doses ranging from 1.5 to 29.2 $\mu g/cm^2$ (for 5.9 $\mu g/cm^2$, HASMC in Fig. 1A and HUVEC in Fig. S8A; for all doses see Fig. S9A for HASMC and Fig. S10A for HUVEC).

Live/Dead staining confirms that cells which retain their unperturbed morphology are indeed alive (Fig. S11). Exposure to ZnO nanoparticles (known to be cytotoxic [65,66]), provides a negative control: HUVEC and HASMC incubated with 5.9 $\mu g/cm^2$ of ZnO were detached and possibly apoptosed (black arrows, Fig. 1A for HASMC, Fig. S10A for HUVEC); at higher ZnO concentrations, it was difficult to find any cells with unmodified morphology (HASMC, Fig. S9B and HUVEC, Fig. S10B). In agreement with the micrographs, a sharp drop in metabolic activity is observed for ZnO at 5.9 $\mu g/cm^2$, and negligible activity remains for cells exposed to higher ZnO concentrations (Fig. 2A and S12C). Results for WSNT and ZnO were confirmed by replicate experiments at 5.9 $\mu g/cm^2$ for three time points (24, 48 and 72 hrs) (Fig. S13). Although no discernible changes in morphology or ratio of live/dead cells was observed for cells exposed to bare WSNT or PLA nanocomposites (relative to media control), there is a measurable decrease in metabolic activity in cells exposed to bare WSNT: approximately 15–20% for 5.9 $\mu g/cm^2$ (for HASMC, Fig. 2A, corresponding to the conditions for the middle micrograph of Fig 1A; for HUVEC, Fig S13B). In contrast, metabolic activity was not significantly reduced by exposure to nanocomposites, relative to PLA (which is significantly lower than for media controls).

3.2 HUVEC and HASMC in direct contact with PLA-WSNT nanocomposites in vitro

Phase contrast micrographs of cells in contact with PLA-WSNT (0.1 wt%) disks for 24 hours show that both HASMCs and HUVECs have similar cell morphology and cell density underneath the disk of PLA-WSNT as they do in the adjacent area free of polymer, as is observed in the case of contact with PLA (Fig. 1B for HASMC; Fig S8B for HUVEC). Surprisingly, all three polymeric samples tested—including the PLA-ZnO negative control —had cell density and morphology underneath and next to the nanocomposite similar to that of their respective media controls (Fig. S8B). Dead (red) and live (green) channel composite micrographs (Fig. 1B and S8B) indicate that all disk treatment conditions have comparable cell viability to the vehicle controls. Cell density appears to be consistent between conditions with only a few dead (red) cells detected. A separate set of samples was used for WST-1 assays of cell metabolic activity as a function of contact with a PLA or nanocomposite disk overlay. A minor but statistically significant drop in metabolic activity was detected in HASMC between the control and PLA. No detectable difference in metabolic activity for either HUVEC or HASMC was found between PLA, PLA-WSNT and PLA-ZnO (Fig. 2A–B for HASMC, Fig. 10C-D for HUVEC). Additionally, these results were confirmed by experiments in which the medium was incubated with PLA nanocomposites for 24 hrs and then applied to cells in culture, which were analyzed at three incubation time points (24, 48 and 72 hrs; Fig. S13).

3.3 TEM of cells exposed to bare WSNT suggests endocytosis and association with cytosolic vesicles

Intrigued by the mild cytotoxic effects of bare WSNT, we looked more closely at the interaction of WSNT with cells using transmission electron microscopy (TEM) of HUVECs and HASMCs treated with bare WSNT. Intracellular aggregates of WSNT appear black; intracellular gray regions are characteristic of protein or nucleic acid concentrations typical of cytoplasm or nuclear contents; intracellular pale gray to white regions correspond to vesicles; and the pale gray observed outside the cells is embedding resin (Fig. S15A, HASMC; Fig. S15B, HUVEC). The majority of intracellular WSNT are visibly associated with vesicles: ~84% (76/91) of the WSNT aggregates in HUVECs and ~85% (55/65) in HASMCs. In many of the TEM micrographs, the WSNT aggregates appear to be incompletely surrounded by vesicles (Fig. S15A-IV, HASMC; Fig. S15B-IV, HUVEC). We attribute this observation to the inherent 3D pleomorphic structure of cellular compartments and the inability of TEM to accurately discern the borders of vesicles in 2D projection images. We were able to perform a small number of tomographic reconstructions to visualize the sample in 3D. Although tomography was limited to a smaller number of WSNT aggregates, the 3D images permit unambiguous delineation of the vesicle border relative to the nanoparticles within it. In these reconstructions, the nanoparticle aggregates appear to be fully enclosed by the associated vesicles in both HASMCs (Movie S1) and HUVECs and (Movie S2).

3.4 Probing the impact on WSNT on the microstructure of PLA during flow

We probe changes in microstructure during and after flow with millisecond time resolution by measuring the optical retardance.

The average retardance is measured using the variations of light intensity transmitted through crossed and parallel polarizers, with the polarizer and analyzer oriented at ± 45° relative to the flow direction and with the laser pointed along the velocity gradient direction [61]. The average retardance is related to the integral of the birefringence over the thickness of the channel [67,68]. Here, there are three contributions to the birefringence: the melt flow birefringence, the birefringence due to formation of oriented PLA crystals and, potentially, the birefringence due to oriented nanotubes.

Comparing the retardance (δ) during the shear pulse (insets of Fig. 3A) for neat PLA and PLA-WSNT nanocomposites reveals that the orientation of nanotubes during flow gives a negligible contribution relative to the melt flow birefringence (the plateau in δ from 1 to 10 s has the same magnitude for the nanocomposites as for neat PLA). After cessation of flow, an initial abrupt decrease in birefringence occurs due to melt relaxation. The optical signature of oriented crystallization (templated by oriented precursors and/or oriented nanotubes) comes later: it is responsible for the increase in retardance that is observed approximately 40 s after inception of shearing. The retardance due to crystallization consistently goes over orders (orders are marked by gray horizontal dashed lines, labelled in Fig. 3A, *left*). Open circles mark the time each order of retardance is reached; the last full order observed is the last data point shown (limited by opacification due to crystallization).

To examine the effect of shearing time (t_s: 10–40 s, Fig. 3A) and shear stress (σ_w: 0.11–0.23 MPa, Fig. 3B), we chose a fixed shearing temperature (T_s = 130 °C) based on a screening study that examined shearing temperatures from 127 to 140 °C (Fig. S16). Flow effects on crystallization were significant at temperature of 133 °C and below, with 130 °C having the advantage that it permits flow for 40 s even at the highest wall shear stress examined (σ_w = 0.23 MPa). The effect of shearing time (at fixed wall shear stress = 0.23 MPa) reveals that WSNT strongly enhance incipient crystallization during the shear pulse, manifested as a sharp increase in retardance above the plateau due to melt flow birefringence. This “upturn” is hardly visible for neat PLA: only a small increase of δ is detected at 35 s for t_s = 40 s (see inset, Fig 3A, *left*). In the literature, an upturn in the retardance is associated with a population of shish that survives melt relaxation and promotes growth of kebabs [68–71] as evidenced by an earlier and strong increase in retardance after cessation of flow (Fig. 3B). As little as 0.05 wt% WSNT enables the upturn to begin in less than 30 s of shearing and to rise 3x greater than the upturn in neat PLA. Increasing the concentration of WSNT to 0.1 wt% further accentuates the upturn. The effect of WSNT during the shear pulse correlates with an important effect of WSNT on the oriented structures (crystallization precursors) that survive after the melt has relaxed (Fig. 3A): in neat PLA, such long-lived oriented structure is only observed for the longest shearing time (nonzero minimum in δ after melt relaxation), whereas 0.05% and 0.1% WSNT enable these structures to form earlier in the shear pulse (30 s for 0.05% and 20 s for 0.1%). After melt relaxation, the subsequent increase in retardance due to crystallization is significantly affected by shearing time and WSNT concentration. In PLA alone, the rate of oriented crystallization increases with t_s. With 0.05 wt% WSNT, even the shortest shearing time give an effect similar to the longest shearing time in PLA alone. Intriguingly, the very steep increase in δ after flow is relatively insensitive to t_s at the highest WSNT concentration (for 0.1 wt%, the time required to reach $\delta = \pi$, 2π, 3π and 4π is nearly independent of t_s, Fig. 3A, *right*). The effect of the wall shear stress ($\boldsymbol{\sigma}_w$) reveals that WSNT decrease the critical stress required for formation of oriented precursors from 0.17 MPa for PLA to 0.13 MPa for PLA-WSNT 0.1 wt% (Fig. 3B). The interaction of shear stress with nanotubes in producing oriented precursors is also evident in the magnitude of the upturn. For example, at $\boldsymbol{\sigma}_w = 0.19$ MPa, the height of the upturn increases 5-fold with addition of 0.1 wt% WSNT (Fig. 4A, *right*). It is interesting to note that for 0.1 wt% WSNT, the very steep rise in δ after cessation of shear become insensitive to shear stress when $\boldsymbol{\sigma}_w \geq 0.19$ MPa and coincides with the behavior that is independent of shearing time at $\boldsymbol{\sigma}_w = 0.23$ MPa (compare Fig. 3A and B, *right*).

PLA and PLA-WSNT samples were extracted from the instrument and microtomed at −35 °C to obtain sections both normal to the flow (sections in the vorticity–velocity gradient plane, denoted by $\nabla \mathrm{x}\mathbf{v}$–$\nabla\mathbf{v}$) and normal to the vorticity direction (sections in the flow–velocity gradient plane, denoted by $\mathbf{v}$–$\nabla\mathbf{v}$) for *ex situ* polarized light microscopy (Fig. 5). For each composition and shearing time the pair of images ($\nabla \mathrm{x}\mathbf{v}$–$\nabla\mathbf{v}$ on the *left* and $\mathbf{v}$–$\nabla\mathbf{v}$ on the *right*) are superficially reminiscent of the classic skin–core morphology observed in injection molding of semicrystalline polymers [72]. However, there is a striking difference: the “oriented skin” is *not* evident in the usual $\mathbf{v}$–$\nabla\mathbf{v}$ plane—it is seen in the $\nabla \mathrm{x}\mathbf{v}$–$\nabla\mathbf{v}$ plane. The center of the sample, which experiences negligible shear, reveals the quiescent nucleating effect of WSNT: neat PLA sections are predominantly amorphous towards the core (indicative of negligible quiescent nucleation prior to removal of the shear cell from the heater block at 1000 s) and PLA-WSNT sections have a completely crystalline, spherulitic core (indicating that WSNT act as heterogenous nucleation sites even in the absence of flow, Fig. 5B–C). Consistent with the *in situ* retardance data (Fig. 3A), we observe an increase in the retardation of the fully solidified samples with increasing t_s (see Michel-Lévy color scale [73] and corresponding retardation below Fig. 5). Intriguingly, the increase in retardation with t_s is more apparent in the plane normal to the flow direction ($\nabla \mathrm{x}\mathbf{v}$–$\nabla\mathbf{v}$, Fig. 5A–C) than in the plane containing the flow direction ($\mathbf{v}$–$\nabla\mathbf{v}$, Fig. 5A–C). For example, in PLA-WSNT 0.05 wt%, increasing t_s results in a thicker birefringent skin that is readily evident in the $\nabla \mathrm{x}\mathbf{v}$–$\nabla\mathbf{v}$ plane (orange-red Michel Lévy color, Fig. 5B), but there is little to no indication of an oriented skin in the $\mathbf{v}$–$\nabla\mathbf{v}$ plane (Fig. 5B). To our knowledge this has not previously been reported for any semicrystalline polymer.

X-ray scattering data acquired along all three projections ($\mathbf{v}$–$\nabla \mathrm{x}\mathbf{v}$, $\nabla \mathrm{x}\mathbf{v}$–$\nabla\mathbf{v}$ and $\mathbf{v}$–$\nabla\mathbf{v}$) confirm the unusual finding that the orientation distribution of crystallites is not symmetric about the flow direction (Fig. 6). The observed WAXS patterns with the beam parallel to $\mathbf{v}$ to probe orientation in the ($\nabla \mathrm{x}\mathbf{v}$–$\nabla\mathbf{v}$)–plane, we observe crystallites with their *c*-axes biased along the $\nabla\mathbf{v}$-direction (Fig. 6B), which may explain the presence of a bright skin viewed in this projection (Fig. 5A–C, *left* image of each pair). In contrast to other semicrystalline polymers, the ($\mathbf{v}$–$\nabla\mathbf{v}$)-plane shows little evidence of a preferred direction of orientation (Fig. 6C), consistent with the absence of a distinct skin in the micrographs (Fig. 5A–C, *right* image of each pair).

3.5 Probing the effect of WSNT on PLA radio-opacity

WS_2 nanotubes embedded in PLA have the potential to increase PLA radio-opacity due to the high atomic number of W respect to C. The X-ray radio-opacity of PLA-WSNT nanocomposites was estimated by measuring the X-ray intensity transmitted by a series of extruded pellets containing a nominal concentration of WSNT equal to 0.1, 0.3, 0.5, 1.0 and 3.0 wt% (Fig. 7A). The decrease of transmitted intensity suggests that a concentration between 0.5 and 1 wt% is sufficient to double the opacity relative to PLA alone.

4. Discussion

WS_2 nanoparticles possess beneficial physical and mechanical properties [44,74] and have recently been studied for various biomedical applications such as friction-reducing agents in nickel-titanium alloys [75] and for reinforcing orthopedic implants [53]. The first step in the use of these nanomaterials for any medical application is to assess their biocompatibility *in vitro*. In a study that explored the use of WSNT to reinforce salivary gland scaffolds, the nanotubes were introduced to rat submandibular gland-derived A5 cells and found to have no effect on the rate of cell proliferation for concentrations up to 35.2 μg/mL [46]. Similarly, another study investigated WSNT biocompatibility in three different cell types (NL-20 human bronchial epithelial cells, human liver-derived HepG2 cells and mouse Raw264 macrophages) and found high cell survival rate with WSNT concentrations of up to 100 μg/mL [47].

In this study, we are interested in interrogating the potential cytotoxicity of WSNT for use in a PLA nanocomposite scaffold that can be inserted into occluded arteries for structural support. Due to the gradual hydrolysis of PLA scaffolds [50], we envision that WSNT in a nanocomposite will gradually be exposed, giving them time to dissolve and be absorbed by the body. Well apposed scaffolds become embedded in vascular endothelial and smooth muscle cells [54]. Therefore, we were encouraged by the observation that short term (24 hrs) direct contact with PLA-WSNT (0.1 wt%) nanocomposites showed no distinguishable effect on either HASMCs or HUVECs relative to PLA (Fig. 1, HASMC and Fig. S8, HUVEC). Comparison of the PLA control to PLA-WSNT in HAMSCs and HUVECs after 24 hours of exposure showed no indication of cytotoxicity in phase contrast microscopy, live/dead staining and WST-1 metabolic assay: a) consistent cell density in the central open area and at the cell-film interface (Fig. S14); b) consistent cell density under the film (Fig. 1B-*left*, HASMC; Fig. S8B–*left*, HUVEC); c) indistinguishable, high viability of cells in the area that was underneath the film (Fig. 1B-*right*, HASMC; Fig. S8B–*right*, HUVEC) and d) comparable metabolic levels as measured by WST-1 assays (Fig. 2B, HASMC; Fig. S12D, HUVEC). Relative to cells that did not have a film placed on them, HASMCs (but not HUVECs) show a small, statistically significant decrease in metabolic activity, independent of WSNT content. Likely causes include reduced nutrient transport due to disk-overlay and/or disruption of cells due to insertion and removal of disks. Based on clinical concerns regarding malapposed scaffolds, future work should examine blood cell cytotoxicity for direct contact with PLA-WSNT (0.1 wt%) nanocomposites.

To the extent that vascular endothelial and smooth muscle cells might be exposed to bare WSNT during bioresorption, we examined direct contact with WSNT. We report the treatment dose in terms of mass per area of cell culture well, as we observed WSNT and ZnO nanoparticles tend to sediment at the bottom of the culture plates. We found that bare WSNT have measurable toxicity in both HAMSCs and HUVECs exposed to doses of 15 μg/cm^2 or more. Metabolic activity relative to controls was not measurably affected by exposure to 5.9 μg/cm^2 WSNT (equivalent to 20 μg/mL; for exposure up to 72 hrs, Fig. S13); but exposure to 14.6 and 29.2 μg/cm^2 decreased metabolic activity by ~11–24% and up to ~32% respectively (Fig. 2A, HASMC; Fig. 10C, HUVEC). Intriguingly, even after direct contact to the highest level of WSNT tested at 29.2 μg/cm^2, we did not observe an abnormal number of floating (dead) cells nor did attached cells have altered morphology or cell density (Fig. S9A and S10A). In addition, intracellular organelles we undisturbed in cells that endocytosed WSNT: cryo-transmission electron micrographs of cells treated with 5.9 μg/cm^2 of WSNT revealed cells with WSNT enclosed within cytosolic vesicles (Fig. S15A, HASMC; Fig. S15B, HUVEC); within the limitations of the image contrast and resolution, based on observation of 65 WSNT aggregates in HASMC cells (Fig. S15A) and 91 WSNT aggregates in HUVEC cells (Fig. S15B), no discernable effect on the nucleus, mitochondria or endoplasmic reticulum was observed. Longer duration hydrolysis studies *in vitro* and bioresorption studies *in vivo* are needed to evaluate the relative rates of dissolution and resorption of WSNT relative to PLA, the extent of exposure of cells to WSNT, and the toxicity of PLA/WSNT relative to PLA itself. As cytotoxic control, we performed the same in-vitro experiments with ZnO nanoparticles (see Supporting Material), known from prior literature to be cytotoxic towards human astrocyte-like U87 cells [66] and human cardiac microvascular endothelial cells [65].

Based on the encouraging results of these biocompatibility assays, we examined the effect of WSNT on morphology development of PLA during processing using short term shear experiments [61,76]. The percentage of nanotubes used in the present work did not bring particular processing difficulty, and equal attention was given to the drying conditions of the neat polymer and the nanocomposites during the several steps of preparation of the ingots to limit degradation induced by residual moisture (as discussed below). The rheo-optical and *ex situ* polarized light micrographs (Fig. 5) reveal a significant feature of PLA itself that was not reported in previous studies of shear-induced crystallization of PLA [77–81]. Specifically, we see a densely nucleated oriented skin even in the PLA without WSNT. Prior literature reports low densities of oriented structure (~50 μm apart) [79–81]. Even in samples in which carbon nanotubes were added to PLA to increase nucleation density, row structures are 10 μm apart. In the present PLA, the spacing between oriented structures is too small to resolve (Fig. 5, left). The formation of a dense skin correlates with a semicrystalline polymer that has low permeability. In PLA, a dense oriented morphology delays hydrolysis [50]. We see three possible causes of the difference in flow-induced crystallization of the present PLA itself. Although we use PLA from the same supplier and with similar D-isomer content (< 2 %) and M_w as many of the prior studies [77–80], we notice that these studies reports > 20% decrease in PLA molecular weight [77] or severe degradation [78] during shear. In contrast, we observe no downward trend in molecular weight or degradation in successive experiments, each of which adds 30–60 min of residence time in the sample reservoir (Fig. S2, S3). Retaining high molecular weight chains offers a plausible explanation of an increase in formation of flow induced oriented precursors. A second possibility is that we may have imposed a higher shear stress than prior studies; unfortunately, prior studies do not report the shear stress [77–81], so we cannot make a meaningful comparison. Lastly, we may reach a higher shear strain due to the stability of pressure driven, rectilinear, short-term shear; in contrast, parallel plate devices lead to flow instability and melt fracture that allows material elements to tear apart and avoid the intended deformation [78].

In addition to the rapid and highly oriented crystallization of PLA, we also observe a fascinating anisotropy in the oriented skin indicating that the structures are not cylindrulites (i.e., they are not isotropic in the plane orthogonal to the flow direction). The PLA-WSNT nanocomposites exaggerate the unusual behavior: nanotubes further enhance rapid, highly oriented crystallization and the peculiar anisotropy in the oriented skin increases (for increasing WSNT content, compare the bottom row in Fig. 5A–C, *left column*).

The remainder of the Discussion is devoted to these intriguing features evident in our data: (1) why does an increase in WSNT concentration reduce the effect of shear time? (2) what is the molecular basis for the unusual morphology observed in the PLA/PLA-WSNT micrographs?

PLA and PLA-WSNT differ in their response to an increase in the shear duration (t_s). For PLA, an increase in t_s increases the slope of the retardance traces after cessation of flow (PLA traces fan out, compare t_s: 10–40 s, Fig. 3A, *left,* 50–200 s). This increase in slope is consistent with the expected effect of increasing t_s: the activation of point-like nuclei that form thread-like precursors continues for the duration of the shear pulse and the initial rate of increase of birefringence after cessation of flow is proportional to the total shish length per unit volume in the oriented skin [68]. The addition of WSNT changes this behavior: the retardance profiles for PLA-WSNT at the end of the shear pulse are more or less unaffected by t_s; the retardance traces are clustered together and have almost identical slopes (see Fig. 3A, *mid–right*). It appears that an increase in t_s has little bearing on the concentration of thread-like precursors; this behavior is reminiscent of “saturation” of shish in isotactic polypropylene (iPP) [69,71]. This saturation effect in the retardance traces manifests in the *ex situ* micrographs as well: with increasing t_s (Fig. 5A, *left*), the degree of anisotropy in the layers near the wall clearly increases in PLA alone, but not for t_s >20s in PLA-WSNT 0.05 wt% (Fig. 5B, *left*) nor for any t_s in PLA-WSNT 0.1 wt% (Fig. 5C, *left*). The effect of WSNT concentration (cf. PLA-WSNT 0.05 wt% and 0.1 wt% retardance post flow, Fig. 3A, *mid–right*) suggests that a concentration of 0.1 wt% has enough oriented nanotubes that any shear-induced oriented precursors have negligible effect: the curves are not only parallel, they are almost indistinguishable for all t_s (Fig. 3BA, *right*). If WSNT are dispersed uniformly, a 0.1 wt% loading of oriented WSNT translates to a spacing of ~ 3.5 μm (see Supporting Material for calculation) between adjacent nanotubes, which makes it likely that the nanotubes act as preexisting oriented structures in the PLA melt. Oriented precursors prevent complete relaxation of retardance after cessation of shear, increase the number of oriented lamellae that subsequently nucleate, and decrease the distance oriented lamellae grow prior to impingement.

The oriented skin in these samples has a feature we have not found in the shear-induced crystallization of any other semicrystalline polymer: a lack of rotational symmetry about the flow direction. To our knowledge, none of the copious literature on skin-core morphologies reports a deviation from rotational symmetry of the crystallites growing outward from the shish. Shear leads to shish that have the chain axis along the flow direction in isotactic polypropylene and polyethylene, among others. Lamellae nucleate on the shish and grow radially outward. Sections cut in the plane of the gradient and vorticity directions (such that the observer is looking down the flow direction, hence the chain axis in the shish) have an oriented skin that appears dark when viewed between crossed polars; this is usually interpreted to mean that the *a*- and *b*- axes are randomly oriented in the plane perpendicular to the *c*-axis [69]. This morphology is referred to as cylindrulitic. Sections cut in the plane of the flow and gradient directions (observer looking along the vorticity axis) have an oriented skin that appears bright when viewed between crossed polarizers, due to the pronounced difference in polarizability along the *c*-axis compared with the *a*- and *b*-axes of the crystal [69].

Electron microscopy on PLA confirms that formation of shish along the flow direction can be induced by shearing the subcooled melt, albeit for relatively long shearing times and high shear strain [72,77]. However, we were unable to find any mention of an unexpected asymmetry about the flow direction. In the present specimens, the pairs of images in the plane of the gradient and vorticity (Fig. 5A–C, *left*) and in the plane of the flow and gradient (see Fig.6A–C, *right*) violate the expectation that the oriented skin on the left should show no retardance (here, a full wave retarder is used, and null retardation would appear first order red/purple). Instead, for each material and each shear time, that is the projection that appears bright—consistently brighter than its partner image in the plane of the velocity and gradient (on the right for each pair of images in Fig. 6). We confirmed that the bright skin seen in ($\nabla \mathrm{x}\mathbf{v}$–$\nabla\mathbf{v}$)-plane is due to preferentially-oriented crystallites and not densely packed spherulites by rotating the sample and observing that the skin appears bright when oriented −45° or 45° relative to the crossed polarizers and dark when it is parallel to them (Fig. S25A–C, *left*). The hypothesis of absence of cylindrical symmetry in the sheared samples is confirmed by the X-ray WAXS data (Fig. 6) with the X-ray beam incident perpendicularly to all three projections of the shear experiments.

The beneficial effect of WSNT on oriented crystallization and nucleation of PLA during shear flow reported in this work has been confirmed also during elongational deformation (tube expansion) of ~80 μm thick extruded tubes [48]. The connection between microstructure and strength for PLA-WSNT tubes in the expanded, crimped and deployed state might open a path toward a future generation of thinner, stronger and radio-opaque scaffolds.

Beyond the observed increase of oriented crystallization, the addition of non-toxic WSNT to PLA may confer intrinsic radio-opacity to the next generation of BVS thanks to the high atomic number of W. PLA has barely no contrast respect to adipose and muscular tissue, therefore the clinically approved BVS is provided with two radio-opaque marks that make the scaffold visible under X-ray irradiation [16]. Our results of X-ray transmission through extruded pellets containing a concentration of WNST between 0.1 and 3.0 wt% (Fig. 7) prove that a small amount as 1 wt% of WSNT is enough to double the PLA radio-opacity respect to higher concentrations of nanoparticles reported in literature (e.g. 5–20 wt% of $BaSO_4$[32]). Further experiments are needed to establish the minimum quantity of WSNT to confer enough contrast to PLA when the scaffold is embedded in deep tissue. PLA-WSNT nanocomposites could be then a valid alternative to the Fantom BVS recently developed by REVA Medical which gains intrinsic radio-opacity from the iodinated diphenol in the Tyrocore™ polymer [82].

5. Conclusions

There is an unmet need for a bioresorbable vascular scaffold (BVS) that has thickness comparable to metal stents (~ 80 μm) for the treatment of lesions in smaller and tortuous arteries. The poor radio-opacity of polymers compared to metals is an added complication as surgeons find it challenging to visualize a BVS with X-rays. Towards the goal of a thinner and radio-opaque BVS, we evaluated tungsten disulfide (WS_2) nanotubes (WSNT) as a candidate additive to polylactide (PLA) to reinforce PLA and confer radio-opacity comparable to clinical standards (e.g., platinum markers). Using cell lines (HUVEC and HASMC) that are relevant to vascular tissue, we assessed the biocompatibility of bare WSNT and PLA-WSNT nanocomposites (0.1 wt%) against appropriate controls. Cells in contact with bare WSNT (up to 29.2 μg/cm^2) and PLA-WSNT films retain their morphology and metabolic activity. Transmission electron micrographs of cells exposed to 5.9 μg/cm^2 WSNT indicate that some nanotubes are endocytosed and appear to be trapped in cytoplasmic vesicles.

The promising *in vitro* biocompatibility of WSNT motivated us to design short term shear experiments that probe the impact of WSNT on oriented crystallization of PLA. *In situ* rheo-optical measurements show that inclusion of 0.1 wt% WSNT reduced both the critical shear duration and the shear stress required for induction of oriented precursors during the short shear pulse. These precursors template oriented crystallization, which has the potential to increase strength in semicrystalline polymers, relevant to the goal of enabling thinner vascular scaffolds.

The results presented in this report suggest that WSNT may be viable reinforcing additives and X-ray contrast agents for biomedical implants. Proposed future biocompatibility studies include *in vivo* testing of the nanocomposite in appropriate animal models. Future *in vitro* experiments may reveal the degradation kinetics and degradation products of WSNT.

Supplementary Material

Refer to Web version on PubMed Central for supplementary material.

Acknowledgements

This research used resources of the Advanced Photon Source (APS), a US Department of Energy (DOE) Office of Science User Facility operated for the DOE Office of Science by Argonne National Laboratory under Contract DE-AC02-06CH11357. We are grateful to the staff of APS beamline 5-D-D, Steven Weigand and James Rix in particular, for their invaluable assistance in acquiring synchrotron X-ray scattering data. We are also indebted to Dan Zhou, a graduate student in the Kornfield group, Dr. Jeremy Wei, a former research scientist in the Kornfield group, and Mark Ladinsky, a scientist at the Caltech electron microscopy core, for their help in microtoming PLA/PLA-WSNT sections and acquiring GPC data and TEM images respectively. This project has received funding from the European Union’s Horizon 2020 research and innovation program under the Marie Skłodowska-Curie grant agreement No 691238, the Jacobs Institute for Molecular Engineering for Medicine at Caltech, the Rosen Center for Bioengineering at Caltech, a National Institutes of Health (NIH) training grant (T32GM112592) and the National Heart, Lung, and Blood Institute of the NIH under Award Number F31HL137308.

References

[1]. World Health Organization, Global Atlas on cardiovascular disease prevention and control, 2011, (n.d.). 10.1016/S0022-3476(51)80275-0.

[2]. Centers for Disease Control and Prevention, Health, United States, (2016) 128. https://www.cdc.gov.

[3]. Hess CN, Huang Z, Patel MR, Baumgartner I, Berger JS, Blomster JI, Fowkes FGR, Held P, Schuyler Jones W, Katona B, Mahaffey KW, Norgren L, Rockhold FW, Hiatt WR, Acute limb ischemia in peripheral artery disease insights from EUCLID, Circulation 140 (2019) 556–565. 10.1161/CIRCULATIONAHA.119.039773. [PubMed: 31238713]

[4]. Behroozian A, Beckman JA, Microvascular disease increases amputation in patients with peripheral artery disease, Arterioscler. Thromb. Vasc. Biol 40 (2020) 534–540. 10.1161/ATVBAHA.119.312859. [PubMed: 32075418]

[5]. Jinnouchi H, Torii S, Sakamoto A, Kolodgie FD, Virmani R, Finn AV, Fully bioresorbable vascular scaffolds: lessons learned and future directions, Nat. Rev. Cardiol 16 (2019) 286–304. 10.1038/s41569-018-0124-7. [PubMed: 30546115]

[6]. Li X, Zhang W, Lin W, Qiu H, Qi Y, Ma X, Qi H, He Y, Zhang H, Qian J, Zhang G, Gao R, Zhang D, Ding J, Long-Term Efficacy of Biodegradable Metal-Polymer Composite Stents after the First and the Second Implantations into Porcine Coronary Arteries, ACS Appl. Mater. Interfaces 12 (2020) 15703–15715. 10.1021/acsami.0c00971. [PubMed: 32159942]

[7]. Li B, Xie Z, Wang Q, Chen X, Liu Q, Wang W, Shen Y, Liu J, Li A, Li Y, Zhang G, Zhang D, Liu C, Wang S, Xie Y, Zhang Z, Ding J, Biodegradable polymeric occluder for closure of atrial septal defect with interventional treatment of cardiovascular disease, Biomaterials 274 (2021) 120851. 10.1016/j.biomaterials.2021.120851. [PubMed: 33965798]

[8]. Epstein AJ, Polsky D, Yang F, Yang L, Groeneveld PW, Coronary revascularization trends in the united states, 2001–2008, JAMA - J. Am. Med. Assoc 305 (2011) 1769–1776. 10.1001/jama.2011.551.

[9]. Ong DS, Jang I-K, Causes, assessment, and treatment of stent thrombosis—intravascular imaging insights, Nat. Rev. Cardiol 12 (2015) 325–336. [PubMed: 25781415]

[10]. Langer R, Tirrell DA, Designing materials for biology and medicine., Nature 428 (2004) 487–492. [PubMed: 15057821]

[11]. Tibbitt MW, Rodell CB, Burdick JA, Anseth KS, Progress in material design for biomedical applications, Proc. Natl. Acad. Sci 112 (2015) 14444–14451. 10.1073/pnas.1516247112. [PubMed: 26598696]

[12]. Zamiri P, Kuang Y, Sharma U, Ng TF, Busold RH, Rago AP, Core LA, Palasis M, The biocompatibility of rapidly degrading polymeric stents in porcine carotid arteries, Biomaterials 31 (2010) 7847–7855. 10.1016/j.biomaterials.2010.06.057. [PubMed: 20696471]

[13]. Ormiston JA, Serruys PW, Onuma Y, van Geuns R-JJ, de Bruyne B, Dudek D, Thuesen L, Smits PC, Chevalier B, McClean D, Koolen J, Windecker S, Whitbourn R, Meredith I, Dorange C, Veldhof S, Hebert KM, Rapoza R, Garcia-Garcia HM, First serial assessment at 6 months and 2 years of the second generation of absorb everolimus-eluting bioresorbable vascular scaffold: a multi-imaging modality study, Circ. Cardiovasc. Interv 5 (2012) 620–632. [PubMed: 23048057]

[14]. Iqbal J, Onuma Y, Ormiston J, Abizaid A, Waksman R, Serruys P, Bioresorbable scaffolds: Rationale, current status, challenges, and future, Eur. Heart J 35 (2014) 765–776. [PubMed: 24366915]

[15]. Serruys PW, Ormiston J, van Geuns R-J, de Bruyne B, Dudek D, Christiansen E, Chevalier B, Smits P, McClean D, Koolen J, Windecker S, Whitbourn R, Meredith I, Wasungu L, Ediebah D, Veldhof S, Onuma Y, A Polylactide Bioresorbable Scaffold Eluting Everolimus for Treatment of Coronary Stenosis: 5-Year Follow-Up, J. Am. Coll. Cardiol 67 (2016) 766–76. [PubMed: 26892411]

[16]. Kossuth MB, Perkins LEL, Rapoza RJ, Design Principles of Bioresorbable Polymeric Scaffolds, Interv. Cardiol. Clin 5 (2016) 349–355. [PubMed: 28582032]

[17]. Serruys PW, Chevalier B, Dudek D, Cequier A, Carrié D, Iniguez A, Dominici M, Van Der Schaaf RJ, Haude M, Wasungu L, Veldhof S, Peng L, Staehr P, Grundeken MJ, Ishibashi Y,

Garcia-Garcia HM, Onuma Y, A bioresorbable everolimus-eluting scaffold versus a metallic everolimus-eluting stent for ischaemic heart disease caused by de-novo native coronary artery lesions (ABSORB II): An interim 1-year analysis of clinical and procedural secondary outcomes from, Lancet 385 (2015) 43–54. 10.1016/S0140-6736(14)61455-0. [PubMed: 25230593]

[18]. Capodanno D, Gori T, Nef H, Latib A, Mehilli J, Lesiak M, Caramanno G, Naber C, Di Mario C, Colombo A, Capranzano P, Wiebe J, Araszkiewicz A, Geraci S, Pyxaras S, Mattesini A, Naganuma T, Münzel T, Tamburino C, Percutaneous coronary intervention with everolimus-eluting bioresorbable vascular scaffolds in routine clinical practice: Early and midterm outcomes from the European multicentre GHOST-EU registry, EuroIntervention 10 (2015) 1144–1153. 10.4244/EIJY14M07-11. [PubMed: 25042421]

[19]. Forrestal B, Lipinski MJ, Bioresorbable Scaffolds: Fading Away or Hope for the Future?, Am. Coll. Cardiol Feb. 7 (2018). https://www.acc.org/latest-in-cardiology/articles/2018/02/07/07/45/bioresorbable-scaffolds.

[20]. Wykrzykowska JJ, Kraak RP, Hofma SH, Van Der Schaaf RJ, Arkenbout EK, IJsselmuiden AJ, Elias J, Van Dongen IM, Tijssen RYG, Koch KT, Baan J, Vis MM, De Winter RJ, Piek JJ, Tijssen JGP, Henriques JPS, Bioresorbable scaffolds versus metallic stents in routine PCI, N. Engl. J. Med 376 (2017) 2319–2328. 10.1056/NEJMoa1614954. [PubMed: 28402237]

[21]. UPDATE on Increased Rate of Major Adverse Cardiac Events Observed in Patients Receiving Abbott Vascular's Absorb GT1 Bioresorbable Vascular Scaffold (BVS) - Letter to Health Care Providers, (2017). https://www.fda.gov/medical-devices/letters-health-care-providers/update-increased-rate-major-adverse-cardiac-events-observed-patients-receiving-abbott-vasculars (accessed April 6, 2020).

[22]. Onuma Y, Serruys PW, Bioresorbable Scaffold, Circulation 123 (2011) 779–797. 10.1161/circulationaha.110.971606. [PubMed: 21343594]

[23]. Gomez-Lara J, Garcia-Garcia HM, Onuma Y, Garg S, Regar E, De Bruyne B, Windecker S, McClean D, Thuesen L, Dudek D, Koolen J, Whitbourn R, Smits PC, Chevalier B, Dorange C, Veldhof S, Morel MA, De Vries T, Ormiston JA, Serruys PW, A comparison of the conformability of everolimus-eluting bioresorbable vascular scaffolds to metal platform coronary stents, JACC Cardiovasc. Interv 3 (2010) 1190–1198. 10.1016/j.jcin.2010.07.016. [PubMed: 21087756]

[24]. Hu Y, Rogunova M, Topolkaraev V, Hiltner A, Baer E, Aging of poly(lactide)/poly(ethylene glycol) blends. Part 1. Poly(lactide) with low stereoregularity, Polymer (Guildf) 44 (2003) 5701–5710. https://www.sciencedirect.com/science/article/pii/S0032386103006141?via%3Dihub (accessed February 10, 2019).

[25]. Banks HT, Hu S, Kenz ZR, A brief review of elasticity and viscoelasticity for solids, Adv. Appl. Math. Mech 3 (2011) 1–51.

[26]. Boland ED, Pawlowski KJ, Barnes CP, Simpson DG, Wnek GE, Bowlin GL, EIectrospinning of bioresorbable polymers for tissue engineering scaffolds, ACS Symp. Ser 918 (2006) 188–204.

[27]. Rathi S, Chen X, Coughlin EB, Hsu SL, Golub CS, Tzivanis MJ, Toughening semicrystalline poly(lactic acid) by morphology alteration, Polymer (Guildf) 52 (2011) 4184–4188. 10.1016/j.polymer.2011.07.032.

[28]. Grijpma DW, Pennings AJ, (Co) polymers of L-lactide, 1. Synthesis, thermal properties and hydrolytic degradation, Macromol. Chem. Phys 195 (1994) 1633–1647.

[29]. Huang MH, Li S, Vert M, Synthesis and degradation of PLA-PCL-PLA triblock copolymer prepared by successive polymerization of ε-caprolactone and DL-lactide, Polymer (Guildf) 45 (2004) 8675–8681.

[30]. Li S, Hydrolytic degradation characteristics of aliphatic polyesters derived from lactic and glycolic acids, J. Biomed. Mater. Res 48 (1999) 342–353. 10.1002/(SICI)1097-4636(1999)48:3<342::AID-JBM20>3.0.CO. [PubMed: 10398040]

[31]. Goonoo N, Bhaw-Luximon A, Rodriguez IA, Wesner D, Schönherr H, Bowlin GL, Jhurry D, Poly(ester-ether)s: III. assessment of cell behaviour on nanofibrous scaffolds of PCL, PLLA and PDX blended with amorphous PMeDX, J. Mater. Chem. B 3 (2015) 673–687. 10.1039/c4tb01350f. [PubMed: 32262350]

[32]. Ang HY, Toong D, Chow WS, Seisilya W, Wu W, Wong P, Venkatraman SS, Foin N, Huang Y, Radiopaque Fully Degradable Nanocomposites for Coronary Stents, Sci. Rep 8 (2018) 1–14. 10.1038/s41598-018-35663-2. [PubMed: 29311619]

[33]. Jakhmola A, Anton N, Anton H, Messaddeq N, Hallouard F, Klymchenko A, Mely Y, Vandamme TF, Poly-ε-caprolactone tungsten oxide nanoparticles as a contrast agent for X-ray computed tomography, Biomaterials 35 (2014) 2981–2986. 10.1016/j.biomaterials.2013.12.032. [PubMed: 24393266]

[34]. Butler TJ, Jackson RW, Robson JY, Owen RJT, Delves HT, Sieniawska CE, Rose JDG, In vivo degradation of tungsten embolisation coils, Br. J. Radiol 73 (2000) 601–603. [PubMed: 10911782]

[35]. Schumacher R, Kampmann C, Wippermann C-F, Brzezinska R, Knuf M, Wenzel A, Abidini M, Habermehl P, Biodegradation of tungsten embolisation coils used in children, Pediatr. Radiol 32 (2003) 839–843.

[36]. Shah Idil A, Donaldson N, The use of tungsten as a chronically implanted material, J. Neural Eng 15 (2018) aaa502. 10.1088/1741-2552/aaa502.

[37]. Peuster M, Kaese V, Wuensch G, Wuebbolt P, Niemeyer M, Boekenkamp R, Fink C, Haferkamp H, Hausdorf G, Dissolution of tungsten coils leads to device failure after transcatheter embolisation of pathologic vessels, Heart 85 (2001) 703–704. https://www.ncbi.nlm.nih.gov/pubmed/11359759.

[38]. Peuster M, Fink C, Von Schnakenburg C, Biocompatibility of corroding tungsten coils: In vitro assessment of degradation kinetics and cytotoxicity on human cells, Biomaterials 24 (2003) 4057–4061. [PubMed: 12834601]

[39]. Peuster M, Fink C, von Schnakenburg C, Hausdorf G, Dissolution of tungsten coils does not produce systemic toxicity, but leads to elevated levels of tungsten in the serum and recanalization of the previously occluded vessel, Cardiol. Young 12 (2002) 229–235. https://www.cambridge.org/core/article/dissolution-of-tungsten-coils-does-not-produce-systemic-toxicity-but-leads-to-elevated-levels-of-tungsten-in-the-serum-and-recanalization-of-the-previously-occluded-vessel/FAF0BFABEFCB3A3028FA201996BA30C2. [PubMed: 12365168]

[40]. Tenne R, Seifert G, Recent Progress in the Study of Inorganic Nanotubes and Fullerene-Like Structures, Annu. Rev. Mater. Res 39 (2009) 387–413. 10.1146/annurev-matsci-082908-145429.

[41]. Zak A, Sallacan-Ecker L, Margolin A, Feldman Y, Popovitz-Biro R, Albu-Yaron A, Genut M, Tenne R, Scaling Up of the WS2 Nanotubes Synthesis, Fullerenes, Nanotub. Carbon Nanostructures 19 (2010) 18–26. 10.1080/1536383X.2010.488594.

[42]. Naffakh M, Marco C, Ellis G, Development of novel melt-processable biopolymer nanocomposites based on poly(l-lactic acid) and WS2 inorganic nanotubes, CrystEngComm 16 (2014) 5062–5072.

[43]. Loffredo F, Tammaro L, Di Luccio T, Borriello C, Villani F, De Vito S, Ramachandran K, Kornfield JA, Effect of tungsten disulfide nanotubes on crystallization of polylactide under uniaxial deformation and annealing, Funct. Compos. Mater 2 (2021). 10.1186/s42252-021-00016-2.

[44]. Shalom H, Kapishnikov S, Brumfeld V, Naveh N, Tenne R, Lachman N, Strong, tough and bio-degradable polymer-based 3D-ink for fused filament fabrication (FFF) using WS2 nanotubes, Sci. Rep 10 (2020) 1–8. 10.1038/s41598-020-65861-w. [PubMed: 31913322]

[45]. Adini AR, Redlich M, Tenne R, Medical applications of inorganic fullerene-like nanoparticles, J. Mater. Chem 21 (2011) 15121.

[46]. Goldman EB, Zak A, Tenne R, Kartvelishvily E, Levin-Zaidman S, Neumann Y, Stiubea-Cohen R, Palmon A, Hovav A-H, Aframian DJ, Biocompatibility of Tungsten Disulfide Inorganic Nanotubes and Fullerene-Like Nanoparticles with Salivary Gland Cells, Tissue Eng. Part A 21 (2015) 1013–1023. 10.1089/ten.tea.2014.0163. [PubMed: 25366879]

[47]. Pardo M, Shuster-Meiseles T, Levin-Zaidman S, Rudich A, Rudich Y, Low Cytotoxicity of Inorganic Nanotubes and Fullerene-Like Nanostructures in Human Bronchial Epithelial Cells: Relation to Inflammatory Gene Induction and Antioxidant Response, Environ. Sci. Technol 48 (2014) 3457–3466. 10.1021/es500065z. [PubMed: 24533583]

[48]. Rocher L, Ylitalo AS, Di Luccio T, Miscioscia R, De Filippo G, Pandolfi G, Villani F, Zak A, Menary GH, Lennon AB, Kornfield JA, Interaction of Poly L-Lactide and Tungsten Disulfide Nanotubes Studied by in Situ X-ray Scattering during Expansion of PLLA/WS2NT Nanocomposite Tubes, Polymers (Basel) 13 (2021) 1764. 10.3390/polym13111764. [PubMed: 34072208]

[49]. Ailianou A, Ramachandran K, Kossuth MB, Oberhauser JP, Kornfield JA, Multiplicity of morphologies in poly (l-lactide) bioresorbable vascular scaffolds, Proc. Natl. Acad. Sci 113 (2016) 11670–11675. 10.1073/pnas.1602311113. [PubMed: 27671659]

[50]. Ramachandran K, Di Luccio T, Ailianou A, Kossuth MB, Oberhauser JP, Kornfield JA, Crimping-induced structural gradients explain the lasting strength of poly l-lactide bioresorbable vascular scaffolds during hydrolysis, Proc. Natl. Acad. Sci (2018) 201807347. 10.1073/pnas.1807347115.

[51]. Xu J-Z, Chen C, Wang Y, Tang H, Li Z-M, Hsiao BS, Graphene Nanosheets and Shear Flow Induced Crystallization in Isotactic Polypropylene Nanocomposites, Macromolecules 44 (2011) 2808–2818.

[52]. Li CY, Li L, Cai W, Kodjie SL, Tenneti KK, Nanohybrid shish-kebabs: Periodically functionalized carbon nanotubes, Adv. Mater 17 (2005) 1198–1202.

[53]. Lalwani G, Henslee AM, Farshid B, Parmar P, Lin L, Qin Y-XX, Kasper FK, Mikos AG, Sitharaman B, Tungsten disulfide nanotubes reinforced biodegradable polymers for bone tissue engineering, Acta Biomater 9 (2013) 8365–8373. 10.1016/j.actbio.2013.05.018. [PubMed: 23727293]

[54]. Wiebe J, Nef HM, Hamm CW, Current Status of Bioresorbable Scaffolds in the Treatment of Coronary Artery Disease, J. Am. Coll. Cardiol 64 (2014) 2541–2551. [PubMed: 25500240]

[55]. Rapoza R, Veldhof S, Oberhauser J, Hossainy SFA, Assessment of a Drug Eluting Bioresorbable Vascular Scaffold, (2015) Patent Appl No. 14/121,435., n.d.

[56]. Bai H, Huang C, Xiu H, Zhang Q, Deng H, Wang K, Chen F, Fu Q, Significantly Improving Oxygen Barrier Properties of Polylactide via Constructing Parallel-Aligned Shish-Kebab-Like Crystals with Well-Interlocked Boundaries, Biomacromolecules 15 (2014) 1507–1514. 10.1021/bm500167u. [PubMed: 24617940]

[57]. Gorrasi G, Pantani R, Hydrolysis and Biodegradation of Poly(lactic acid), in: Synth. Struct. Prop. Poly(Lactic Acid), Springer International Publishing AG 2017, 2017: pp. 1507–1514. 10.1007/12.

[58]. Mastronarde DN, Automated electron microscope tomography using robust prediction of specimen movements., J. Struct. Biol 152 (2005) 36–51. [PubMed: 16182563]

[59]. Kremer JR, Mastronarde DN, McIntosh JR, Computer visualization of three-dimensional image data using IMOD., J. Struct. Biol 116 (1996) 71–76. [PubMed: 8742726]

[60]. Mastronarde DN, Correction for non-perpendicularity of beam and tilt axis in tomographic reconstructions with the IMOD package., J. Microsc 230 (2008) 212–217. [PubMed: 18445149]

[61]. Kumaraswamy G, Verma RK, Kornfield JA, Novel flow apparatus for investigating shear-enhanced crystallization and structure development in semicrystalline polymers, Rev. Sci. Instrum 70 (1999) 2097–2104.

[62]. Lilly B, We Have Contact: Endothelial Cell-Smooth Muscle Cell Interactions, Physiology 29 (2014) 234–241. [PubMed: 24985327]

[63]. Foglia S, Ledda M, Fioretti D, Iucci G, Papi M, Capellini G, Lolli MG, Grimaldi S, Rinaldi M, Lisi A, In vitro biocompatibility study of sub-5 nm silica-coated magnetic iron oxide fluorescent nanoparticles for potential biomedical application, Sci. Rep 7 (2017) 1–13. [PubMed: 28127051]

[64]. Appel JH, Li DO, Podlevsky JD, Debnath A, Green AA, Wang QH, Chae J, Low Cytotoxicity and Genotoxicity of Two-Dimensional MoS 2 and WS 2, ACS Biomater. Sci. Eng 2 (2016) 361–367. [PubMed: 33429540]

[65]. Sun J, Wang S, Zhao D, Hun FH, Weng L, Liu H, Cytotoxicity, permeability, and inflammation of metal oxide nanoparticles in human cardiac microvascular endothelial cells: Cytotoxicity, permeability, and inflammation of metal oxide nanoparticles, Cell Biol. Toxicol 27 (2011) 333–342. [PubMed: 21681618]

[66]. Leung SW, Lai JCK, Lai MB, Jandhyam S, Dukhande VV, Bhushan A, Daniels CK, Leung SW, Exposure to titanium dioxide and other metallic oxide nanoparticles induces cytotoxicity on human neural cells and fibroblasts, Int. J. Nanomedicine 3 (2008) 533. [PubMed: 19337421]

[67]. Fernandez-Ballester L, Thurman DW, Kornfield JA, Real-time depth sectioning: Isolating the effect of stress on structure development in pressure-driven flow, J. Rheol. (N. Y. N. Y) 53 (2009) 1229–1254. 10.1122/1.3164970.

[68]. Fernandez-Ballester L, Thurman DW, Zhou W, Kornfield JA, Effect of long chains on the threshold stresses for flow-induced crystallization in iPP: Shish kebabs vs sausages, Macromolecules 45 (2012) 6557–6570.

[69]. Kumaraswamy G, Issaian AM, Kornfield JA, Shear-enhanced crystallization in isotactic polypropylene. 1. Correspondence between in situ rheo-optics and ex situ structure determination, Macromolecules 32 (1999) 7537–7547.

[70]. Kumaraswamy G, Kornfield JA, Yeh F, Hsiao BS, Shear-enhanced crystallization in isotactic polypropylene. 3. Evidence for a kinetic pathway to nucleation, Macromolecules 35 (2002) 1762–1769.

[71]. Kornfield JA, Kumaraswamy G, Issaian AM, Recent Advances in Understanding Flow Effects on Polymer Crystallization, Ind. Eng. Chem. Res (2002) 6383–6392.

[72]. Xu H, Zhong G, Fu Q, Lei J, Jiang W, Hsiao BS, Li Z, Formation of Shish-Kebabs in Injection-Molded Poly(L-Lactic acid) by Application of an Intense Flow Field, Appl. Mater. Interfaces 4 (2012) 6774–6784.

[73]. Sørensen BE, A revised Michel-Lévy interference colour chart based on first-principles calculations, Eur. J. Mineral 25 (2013) 5–10. http://openurl.ingenta.com/content/xref?genre=article&issn=0935-1221&volume=25&issue=1&spage=5.

[74]. Kaplan-Ashiri I, Cohen SR, Gartsman K, Ivanovskaya V, Heine T, Seifert G, Wiesel I, Wagner HD, Tenne R, On the mechanical behavior of WS2 nanotubes under axial tension and compression, Proc. Natl. Acad. Sci 103 (2006) 523–528. [PubMed: 16407141]

[75]. Samorodnitzky-Naveh GR, Redlich M, Rapoport L, Feldman Y, Tenne R, Inorganic fullerene-like tungsten disulfide nanocoating for friction reduction of nickel-titanium alloys., Nanomedicine 4 (2009) 943–950. [PubMed: 19958230]

[76]. Janeschitz-Kriegl H, Poylmer Melt Rheology and Flow Birefringence, Springer-Verlag, 1983. 10.1007/978-3-642-68822-5.

[77]. Bojda J, Piorkowska E, Shear-induced nonisothermal crystallization of two grades of PLA, Polym. Test 50 (2016) 172–181. 10.1016/j.polymertesting.2016.01.006.

[78]. Xu H, Xie L, Hakkarainen M, Beyond a Model of Polymer Processing-Triggered Shear: Reconciling Shish-Kebab Formation and Control of Chain Degradation in Sheared Poly(l-lactic acid), ACS Sustain. Chem. Eng 3 (2015) 1443–1452.

[79]. Zhong Y, Fang H, Zhang Y, Wang Z, Yang J, Wang Z, Rheologically determined critical shear rates for shear-induced nucleation rate enhancements of poly(lactic acid), ACS Sustain. Chem. Eng 1 (2013) 663–672.

[80]. Tang H, Bin Chen J, Wang Y, Xu JZ, Hsiao BS, Zhong GJ, Li ZM, Shear flow and carbon nanotubes synergistically induced nonisothermal crystallization of poly(lactic acid) and its application in injection molding, Biomacromolecules 13 (2012) 3858–3867. [PubMed: 23072455]

[81]. Yamazaki S, Itoh M, Oka T, Kimura K, Formation and morphology of “shish-like” fibril crystals of aliphatic polyesters from the sheared melt, Eur. Polym. J 46 (2010) 58–68. 10.1016/j.eurpolymj.2009.09.003.

[82]. Chevalier B, Abizaid A, Carrié D, Frey N, Lutz M, Weber-Albers J, Dudek D, Weng SC, Akodad M, Anderson J, Stone GW, Clinical and Angiographic Outcomes with a Novel Radiopaque Sirolimus-Eluting Bioresorbable Vascular Scaffold: The FANTOM II Study, Circ. Cardiovasc. Interv 12 (2019) 1–8. 10.1161/CIRCINTERVENTIONS.118.007283.

Significance:

Bioresorbable Scaffolds (BRSs) support regeneration of arteries without permanent mechanical constraint. Poly-L-lactide (PLLA) is the structural material of the first approved BRS for coronary heart disease (ABSORB BVS), withdrawn due to adverse events in years 1–3. Here, we examine tungsten disulfide (WS_2) nanotubes (WSNT) in PLA to address two contributors to early complications: (1) reinforce PLLA (enable thinner BRS), and (2) increase radiopacity (provide intraoperative visibility). For BRS, it is significant that WSNT disperse, remain dispersed, reduce friction and improve mechanical properties without additional chemicals or surface modifications. Like WS_2 nanospheres, bare WSNT and PLA-WSNT nanocomposites show low cytotoxicity *in vitro*. PLA-WSNT show enhanced flow-induced crystallization relative to PLA, motivating future study of the processing behavior and strength of these materials.

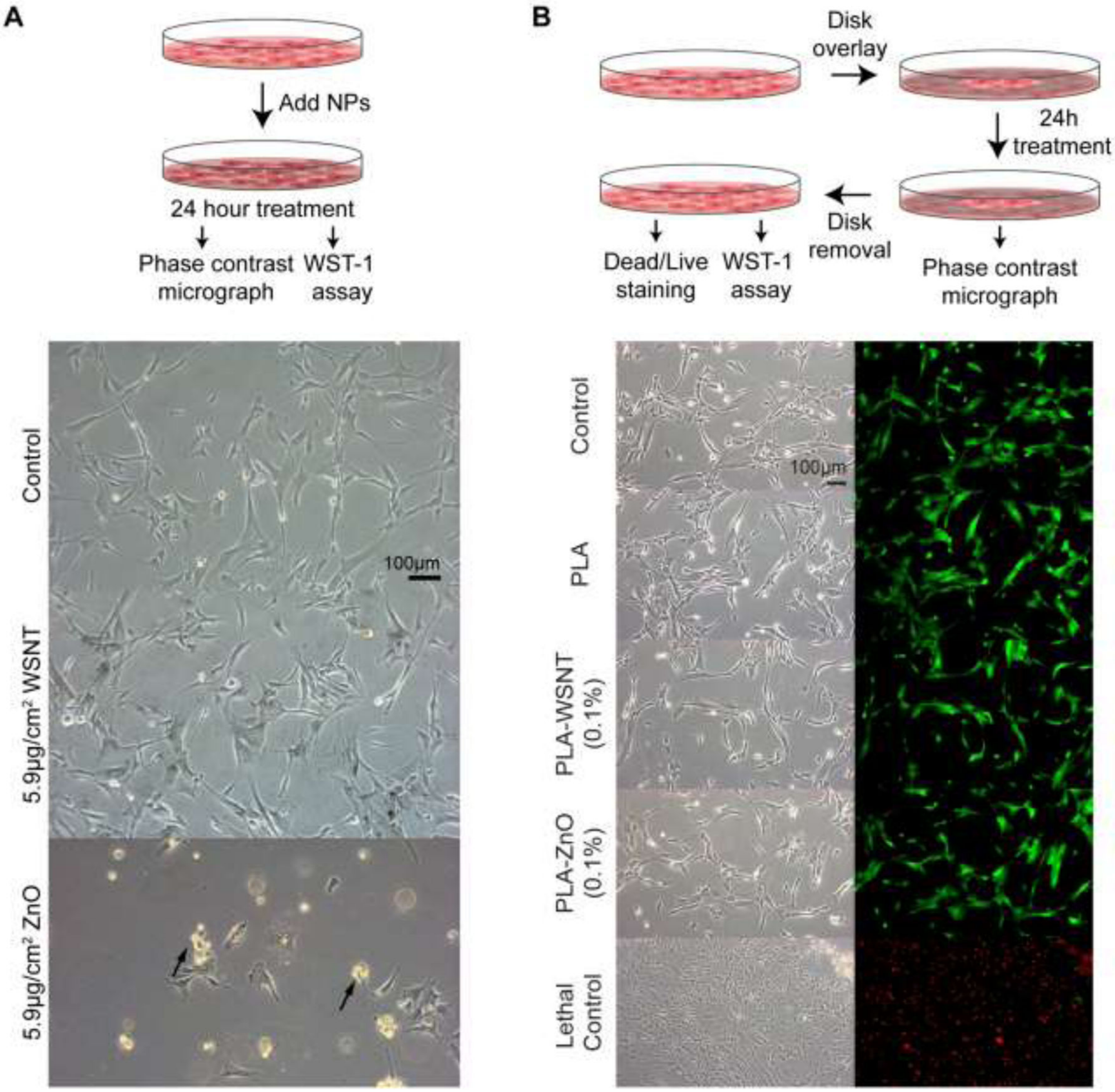

Fig. 1.

(**A**) *Top*: Schematic illustrating that cells are treated with varying concentrations of WSNT or ZnO nanoparticles for 24 hours. *Bottom*: Phase contrast microscopy images (scale bar shown in control) of HASMC incubated in direct contact with 5.9 μg/cm^2 WSNT or ZnO nanoparticles (see Fig. S8A for HUVEC; for all doses from 1.5 to 29.2 μg/cm^2, see Fig. S9 HASMC and Fig. S10 HUVEC). (**B**) *Top*: Schematic of cells treated with nanocomposite polymer disks for 24 hours in 12-well plates. *Bottom:* Phase contrast micrographs (*left*) and merged live (green) and dead (red) stained images (*right*) of HASMC cells in the region underneath the nanocomposite (see Fig. S8B for HUVEC). (Scale bar shown in first phase contrast image)

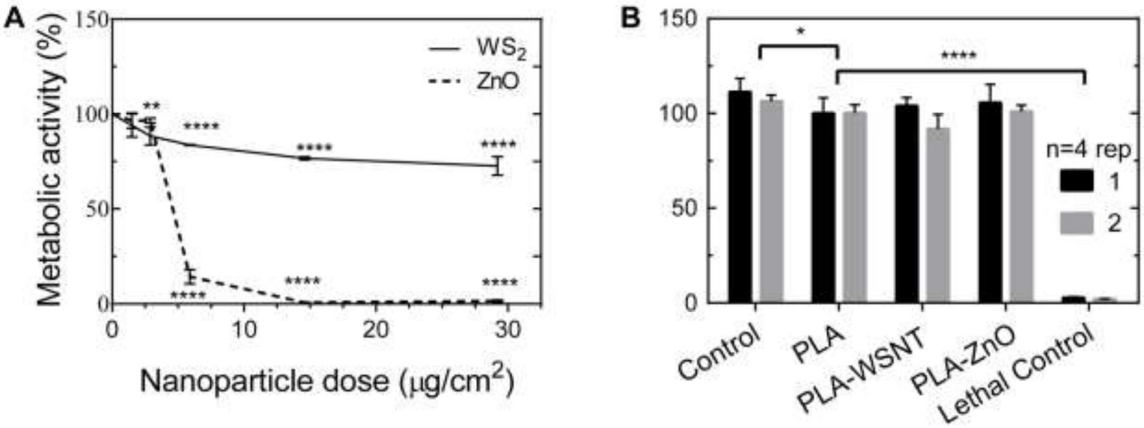

Fig. 2.

(**A**) Cells exposed to direct contact with WSNT (see scheme in Fig.1A, top) showed a moderate drop in metabolic activity (here, HASMC cells; HUVEC in Fig S12C). Direct contact with ZnO induced strong cytotoxicity at nominal dose ≥ 5.9 μg/cm^2. Mean and standard error of mean plotted. All statistical tests were performed against control samples; stars indicate the magnitude of adjusted p-value (* P≤0.05, ** P≤0.01, ***P≤0.001, **** P≤0.0001). (**B**) Cellular metabolic activity levels, inferred from the WST-1 assay (see scheme in Fig. 1B, top), show no statistical difference in viability between HASMC cells treated with PLA disks and PLA nanocomposite (0.1% of WSNT or ZnO) disks (see Fig. S12D for HUVEC). Experiments were performed twice with four replicates per condition. Experiment-specific mean and standard deviation are plotted. All statistical tests were performed against the PLA condition; stars indicate the magnitude of adjusted p-value (* P≤0.05, ** P≤0.01, *** P≤0.001, **** P≤0.0001).

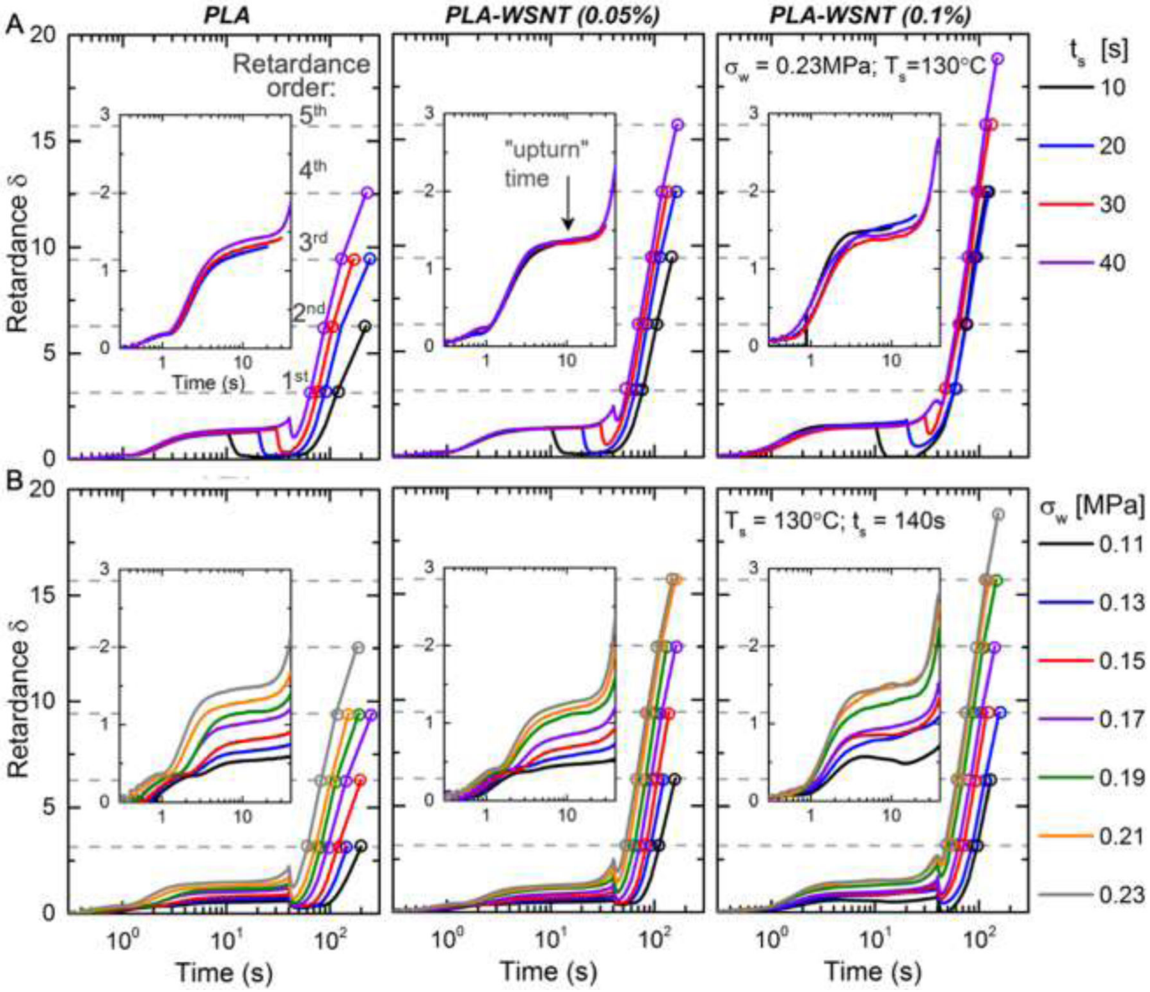

Fig. 3.

In situ retardance (δ) profiles during and after cessation of flow for (*left*) PLA, (*mid)* PLA-WSNT (0.05 wt%) and (*right*) PLA-WSNT 0.1 wt% subjected to varying (**A**) shear duration (t_S: 10 to 40 s) at matched shear temperature 130 °C and shear stress 0.23 MPa (Fig. S17B) and (**B**) wall shear stress (σ_W: 0.11 to 0.23 MPa) at matched shear temperature 130 °C and shear time 40 s (Fig. S17C); dependence on the shear temperature is reported in Fig. S16. In (A), the wall shear rate is ~ 0.35 s^{-1} for all cases; and in (B), the wall shear rate increases from ~ 0.19 s^{-1} at 0.11 MPa to ~ 0.35 s^{-1} at 0.23 MPa. The wall shear rate is calculated from the extruded material (Fig. S18A) and the Rabinowitsch correction (equations S2–S4) is applied to account for non-Newtonian flow (Fig. S18B). The onset of an "upturn" in the retardance during flow is indicated by a black arrow in (A, *mid*). Quantitative characteristics of the upturn for PLA and PLA-WSNT are presented in Fig. 5. The dashed horizontal gray lines indicate the order of retardance, which follows integer multiples of π (e.g. 1st order: $\delta = \pi$; 2nd order: $\delta = 2\pi$ and so on). The retardance is calculated from normalized intensity traces presented in Figs. S19–S21. The extruded material from each condition was subject to gel permeation chromatography (GPC) measurements that indicated little to no change in molecular weight for the experiments in A-B (Figs. S2–S3).

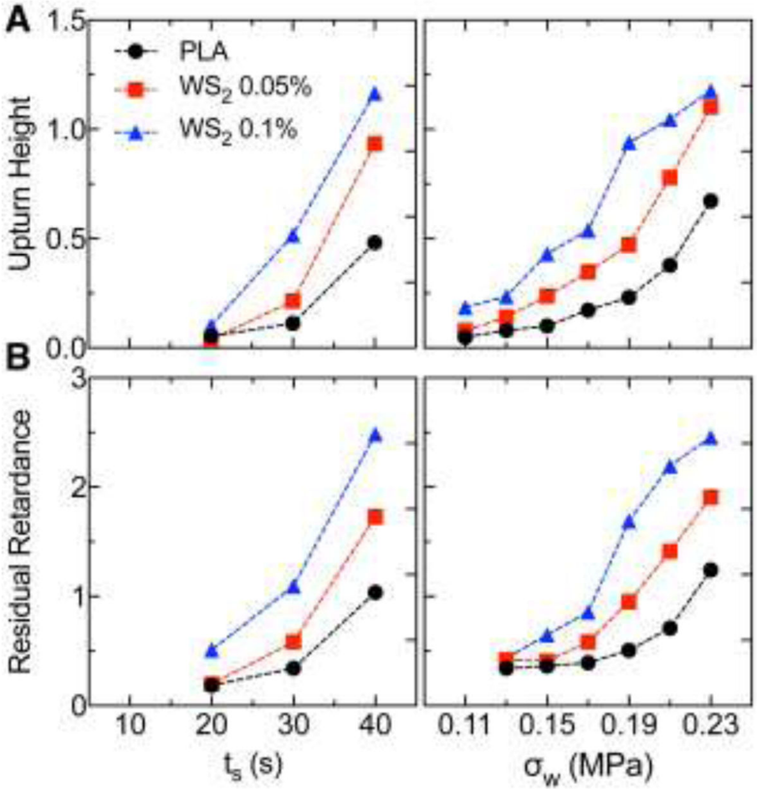

Fig. 4.

In situ retardance traces of PLA and PLA-WSNT were analyzed to compute (**A**) the "upturn height", *i.e.*, retardance at the upturn time (defined in the inset of Fig. 3B) and (**B**) the residual retardance after cessation of flow as a function of (*left*) shear duration (see Fig. 3B) and (*right*) wall shear stress (see Fig. 3C). We describe the calculation of the upturn height and residual retardance in the SM (Figs. S22).

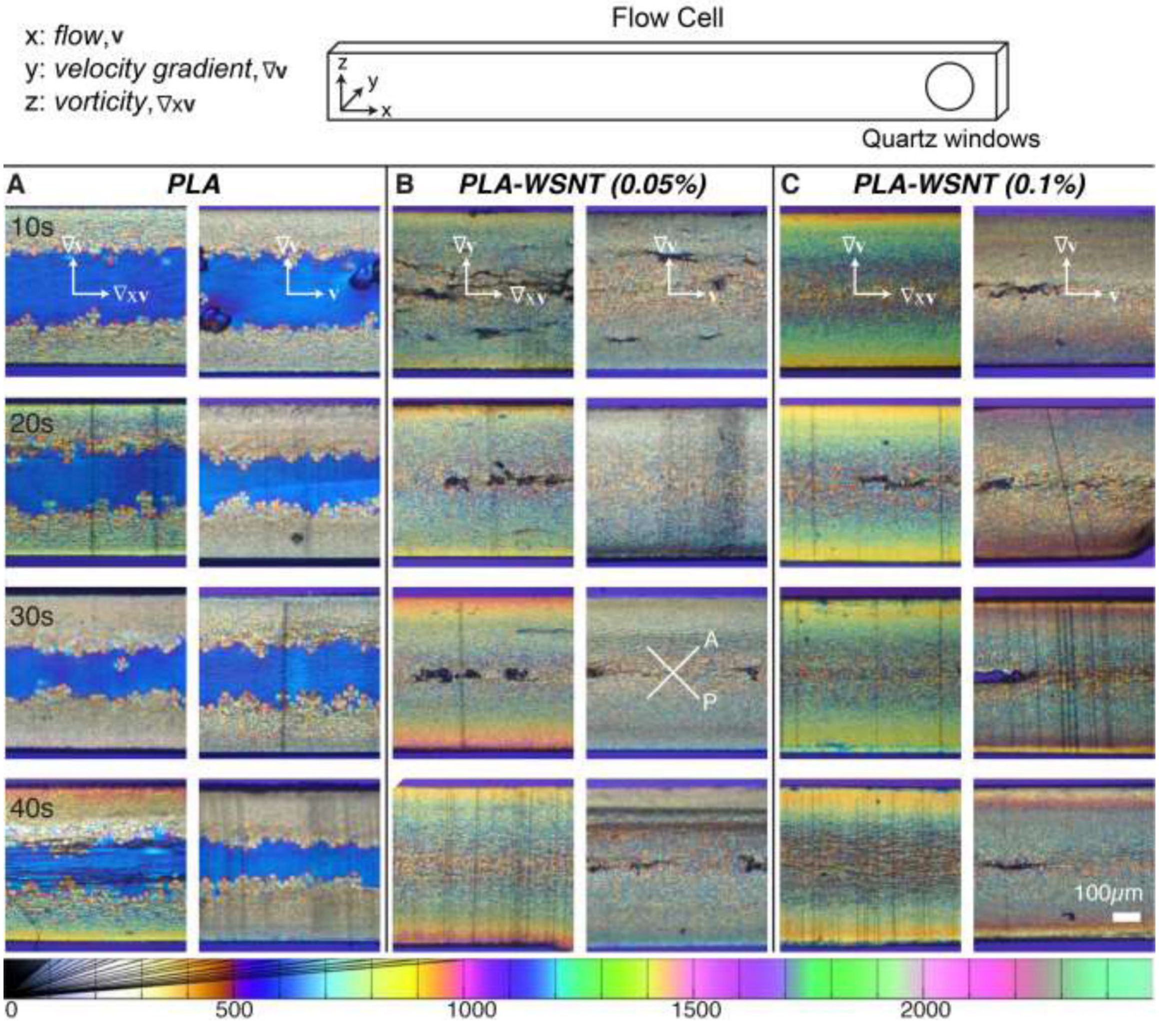

Fig. 5.

Polarized light micrographs of ~ 50 μm thick sections from samples sheared for t_s from 10 to 40 s at T_s = 130 °C and σ_w = 0.23 MPa for (**A**) PLA, (**B**) PLA-WSNT (0.05 wt%) and (**C**) PLA-WSNT (0.1 wt%). For each composition, pairs of images are displayed: the first column (A-C, *left*) presents micrographs of sections cut normal to the flow direction (vorticity – velocity gradient plane, labelled as ∇x**v**–∇**v**, see scheme of the flow cell on top) and the second column (A-C, *right)* presents micrographs of sections cut normal the vorticity direction (flow – velocity gradient plane, labelled as **v**–∇**v**, see scheme of the flow cell on top). Images are acquired through linear crossed polarizers, analyzer (A) and polarizer (P) orientations are indicated in **(B)** 30 s, *right*), with a full-wave retardation plate inserted (slow axis vertical, see Fig. S24 for details). The Michel-Lévy color chart at the bottom (adapted from Ref. [68]) relates colors to retardation in nm.

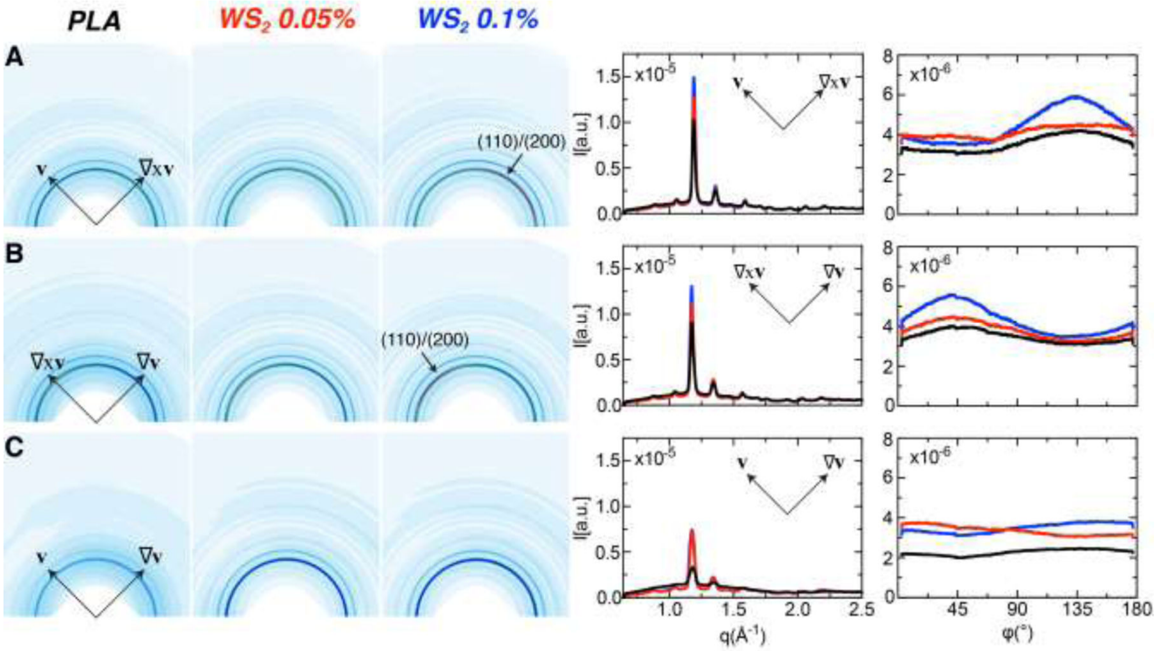

Fig. 6.

Wide Angle X-ray Scattering (WAXS) data acquired on PLA, PLA-WSNT 0.05 wt% and PLA-WSNT 0.1 wt% samples sheared at T_s = 130 °C, t_s = 40 s and $\boldsymbol{\sigma}_w$ = 0.21 MPa. For each sample, the microstructure was probed along all three projections (defined in Fig. 5, top): (**A**) flow – vorticity (**v**–∇x**v**), (**B**) vorticity – velocity gradient (∇x**v**–∇**v**) and (**C**) flow – velocity gradient (**v**–∇**v**). The WAXS data are presented as (*left*) 2D patterns, and (*right*) intensity plots I(*q*) and I(*φ*) of the (110)/(200) diffraction peak, where I(*q*) is azimuthally averaged and I(*φ*) is averaged over $1.13 \leq q \leq 1.23$ Å^{-1} (colors correspond to labels above 2D patterns). The intensity plots use colors to distinguish neat PLA, PLA-WSNT 0.05wt% and PLA-WSNT 0.1wt% (black, red and blue respectively). The WAXS patterns are presented using a custom colormap that varies from 0 [white] to 1.75e^{-5} [red] counts/(total counts). X-ray data acquired for samples sheared at lower wall shear stresses (σ_w = 0.11 and 0.15 MPa) are presented in the SI (see Figs. S26 – S28).

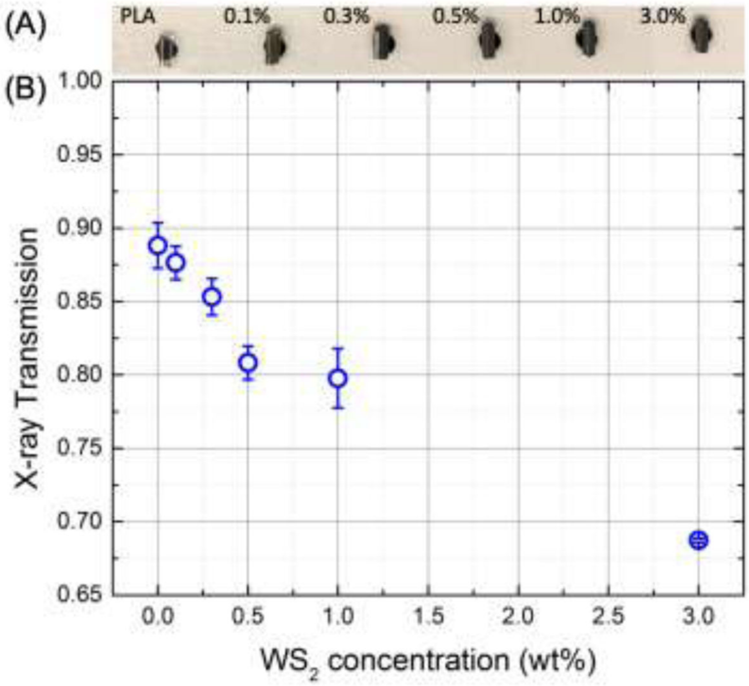

Fig. 7.

X-ray radio-opacity evaluated from the transmitted beam intensity during SAXS/WAXS experiments on PLA and PLA-WNSNT extruded pellets (A) containing increasing concentration of WSNT (from 0.1 to 3 wt%).